JM PAPERS

Spectral analysis of the net turbulent force in accelerating turbulent pipe flow

Byron Guerrero[1,2] (iD), **Martin F. Lambert**[3] (iD) **and Rey C. Chin**[1] (iD)

[1]School of Electrical and Mechanical Engineering, University of Adelaide, Adelaide, SA 5005, Australia

[2]Departamento de Ciencias de la Energía y Mecánica, Universidad de las Fuerzas Armadas - Espe Sangolquí-Ecuador, Adelaide, Australia

[3]School of Civil Engineering and Architecture, University of Adelaide, Adelaide, SA 5005, Australia

Corresponding author: Byron Guerrero, byron.guerrerohinojosa@adelaide.edu.au

This investigation examines the dynamic response of an accelerating turbulent pipe flow using direct numerical simulation data sets. A low/high-pass Fourier filter is used to investigate the contribution and time dependence of the large-scale motions (LSM) and the small-scale motions (SSM) into the transient Reynolds shear stress. Additionally, it analyses how the LSM and SSM influence the mean wall shear stress using the Fukagata–Iwamoto–Kasagi identity. The results reveal that turbulence is frozen during the early flow excursion. During the pretransition stage, energy growth of the LSM and a subtle decay in the SSM is observed, suggesting a laminarescent trend of SSM. The transition period exhibits rapid energy growth in the SSM energy spectrum at the near-wall region, implying a shift in the dominant contribution from LSM to SSM to the frictional drag. The core-relaxation stage shows a quasisteady behaviour in large- and small-scale turbulence at the near-wall region and progressive growth of small- and large-scale turbulence within the wake region. The wall-normal gradient of the Reynolds shear stress premultiplied energy cospectra was analysed to understand how LSM and SSM influence the mean momentum balance across the different transient stages. A relevant observation is the creation of a momentum sink produced at the buffer region in large- and very large-scale (VLSM) wavelengths during the pretransition. This sink region annihilates a momentum source located in the VLSM spectrum and at the onset of the logarithmic region of the net-force spectra. This region is a source term in steady wall-bounded turbulence.

Key words: pipe flow, turbulence simulation, turbulent transition

1. Introduction

Turbulent pipe flows have been studied for approximately 140 years, starting from the seminal investigation conducted by Reynolds (1883). Most experimental, theoretical and numerical investigations in wall-bounded flows have predominantly focused in unveiling the flow physics and universal laws under steady conditions. In the context of this paper, the word 'steady' is referred to as constant flow rate. Existing studies on canonical wall-bounded turbulence (i.e. pipe, channel and boundary layer) have provided significant insights for estimating essential flow quantities, such as the mean skin friction coefficient. Accurate prediction of this coefficient is crucial for practitioners to quantify energy dissipation due to frictional drag in fluid transportation systems operating under steady or quasisteady conditions.

Nonetheless, real-world fluid transportation systems, both technological and biological, rarely operate under steady conditions. In industrial pipe flows, for example, the flow rate is often modulated by control valves or pumping systems to meet varying system demands, leading to frequent accelerations and decelerations. In this regard, several one-dimensional models $f(x, t)$ have been developed to predict the unsteady friction (Zielke 1968; Vardy & Brown 1995, 2003). While these one-dimensional approximations have become a useful tool to predict the time dependence of the frictional drag accelerating/decelerating flows, they do not explicitly consider the wall-normal variations in the flow quantities and the three-dimensional effects of sudden changes in the pressure gradient into the flow physics and the flow structures.

In this line, efforts have been made to establish unsteady Reynolds-averaged Navier–Stokes closure models based on the turbulent viscosity or eddy viscosity approach for unsteady pipe flows (Scotti & Piomelli 2001). However, most of these approaches consider that the growth or decay in the Reynolds shear stress or the eddy viscosity is in phase with the imposed change in the flow rate (Liu *et al.* 2024). Nonetheless, experimental (He & Jackson 2000) and numerical studies (Vardy *et al.* 2015; He, Seddighi & He 2016; Mathur *et al.* 2018; Guerrero *et al.* 2022, 2023) have shown that the eddy viscosity presents a phase lag with the change in the bulk velocity in linearly accelerating and decelerating flows.

In spite of the efforts mentioned above, there is a gap in the literature regarding the characteristics of the flow structures present during the transient process occurring in accelerating pipe flows. This paper, therefore, aims to bridge this gap by extending the current understanding of accelerating turbulent pipe flows from a structural point of view. Specifically, it examines the evolution of the different scales of turbulence across the different transient stages. Direct numerical simulation (DNS) datasets from Guerrero, Lambert & Chin (2021) have been utilised to conduct a series of spectral analyses of different flow quantities such as the Reynolds shear stress, the velocity–vorticity correlations and the net-force spectra (Guala, Hommema & Adrian 2006).

1.1. *Literature review*

1.1.1. *Delayed turbulence and laminarescent trend*

One of the interesting characteristics of accelerating turbulent pipe flows is that turbulence generation and propagation experience a delay concerning the increase in the flow rate (Maruyama, Kuribayashi & Mizushina 1976). In fact, during the early flow excursion, turbulence exhibits a 'frozen' behaviour. In other words, the stress tensor remains invariant for a short time. Later, a second delay exists associated with the diffusion of 'new' vorticity from the wall towards the pipe centreline. He & Jackson (2000) conducted three-beam, two-component laser Doppler anemometry (LDA) experiments to analyse turbulent pipe

flows subjected to a finite ramp-up acceleration. The results from that study revealed that aside from the two delays observed by (Maruyama *et al.* 1976), a third delay was associated with turbulence kinetic energy redistribution across the three orthogonal components. Indeed, the study mentioned above explains that the streamwise normal stress $\langle u_z u_z \rangle$ responds earlier than the azimuthal $\langle u_\theta u_\theta \rangle$ and the wall-normal stresses $\langle u_y u_y \rangle$, where u stands for the velocity fluctuation, and the subscripts z, θ and y are the streamwise, azimuthal and wall-normal components, respectively. Within that context, He & Jackson (2000) proposed a dimensionless parameter $\gamma = [(\mathrm{d}U_b/\mathrm{d}t)(1/U_{b0})(D/u_{\tau 0})]$, where U_b is the average velocity, u_τ is the friction velocity and D is the pipe diameter. They also determined that as $\gamma \gg 1$, the turbulent energy deviates from its quasisteady value. Similar parameters have been proposed in the context of accelerating and decelerating flow based on dimensional analyses (Ariyaratne, He & Vardy 2010; Jung & Kim 2017).

Greenblatt & Moss (1999) investigated accelerating turbulent pipe flows at low ramp gradients. This investigation utilised single-component LDA experiments alongside numerical simulations employing the Reynolds-averaged Navier–Stokes approach with different eddy viscosity models. It should be noted that this study was conducted only during the ramp-up time. The findings from that study revealed that the streamwise turbulence intensity at the near-wall region decayed during the early flow excursion, showing a trend to relaminarisation owing to the change imposed in the pressure gradient. Complementing this research, Greenblatt & Moss (2004) investigated the response during rapid ramp-up and the transient relaxation of fully developed turbulent pipe flows at high Reynolds numbers (from $Re_{b,0} \approx 31\,000$ up to $Re_{b,1} \approx 82\,000$) using single-component LDA. Their results indicated that rapidly accelerating pipe flows followed three transient stages until they relaxed towards their final steady state. This conclusion was based on the behaviour observed in integral quantities such as the displacement thickness (δ^*) and the shape factor (H) on a time scale normalised by the ramp-up duration (T).

In addition to the delayed turbulence response, Sreenivasan (1982) investigated spatially accelerating turbulent boundary layers and explained that with an increasing pressure gradient, there emerges an initial region where standard turbulent statistics, such as the mean velocity profile and the components of the Reynolds stress tensor, remain invariant, consistent with the frozen behaviour observed during early flow excursions as explained by Maruyama *et al.* (1976). Sreenivasan (1982) further illustrates that beyond this phase of frozen turbulence, the flow exhibits a 'laminarescent' behaviour, indicating a tendency towards relaminarisation without implying a complete transition to laminar flow. Subsequently, as the acceleration reduces, the flow undergoes retransition to turbulence. It is noteworthy that the results observed by Sreenivasan (1982) compared with temporally accelerated flows show substantial similarities. Indeed, a recent numerical investigation of spatially accelerating in a channel flow using a moving-wall as a boundary condition (Falcone & He 2022) demonstrated similarities in the transient turbulence response among spatially and temporally accelerating wall-bounded flows.

1.1.2. *Perturbation boundary layer*

Another interesting feature observed in accelerating flows is associated with generating a perturbation laminar boundary layer superimposed on the turbulent base flow. Kurokawa & Morikawa (1986) conducted a series of hot-wire anemometry measurements in accelerating and decelerating turbulent pipe flow. Their findings suggested that when the acceleration is significantly large compared with the time required by the viscous effects to propagate to the outer flow region (i.e. $\gamma \gg 1$), the velocity profile during the early flow excursion appears to consist of a potential core surrounded by a narrow boundary layer

close to the wall. As the flow establishes, the boundary layer develops and the viscous effects propagate towards the pipe centreline. However, a distinct behaviour was observed in the development of the mean velocity profile under mild acceleration rates.

Following those lines, other experimental, numerical and theoretical studies have been developed based on this concept. Indeed, it has been demonstrated that for rapidly accelerating pipe and channel flows, the mean velocity profile during the early flow excursion can be understood as the addition of the mean velocity profile of the base flow plus a plug-like inflow, which, as time progresses develops as a perturbation boundary layer (He & Seddighi 2015; Mathur *et al.* 2018). In other words, the perturbation boundary layer can be computed as $\langle U^{\wedge}(y, t) \rangle = \langle U(y, t) \rangle - \langle U(y, 0) \rangle / \langle U_c(t) - U_c(0) \rangle$, where U stands for the streamwise velocity of the pipe or the channel and U_c is the centreline velocity. This perturbation boundary layer is extremely thin at the onset of the early flow excursion and significantly increases the viscous shear stress (He & Seddighi 2013; Guerrero *et al.* 2021).

Moreover, recent studies have shown that during the early flow excursion, the mean velocity profile of the developing boundary layer can be accurately represented by the solution of Stoke's first problem (He & Seddighi 2015). Further investigations into this concept resulted in analytical solutions of the perturbation boundary layer mean profile, displacement thickness and centreline velocity (Joel Sundstrom & Cervantes 2017). Furthermore, the solution of the perturbation boundary layer based on Stoke's first problem has been extended to decelerating flows, revealing substantial similarities in $\langle U^{\wedge} \rangle$ across the early flow excursion in both accelerating and decelerating flow (Mathur 2016; Joel Sundstrom & Cervantes 2018).

1.1.3. *Numerical studies of accelerating flow*

Numerical simulations of the Navier–Stokes equations have become a valuable tool to unveil the three-dimensional physics of wall-bounded turbulence due to the difficulties of experimentally sampling accurate velocity signals at the near-wall region of a turbulent wall-bounded flow. In that regard, the early 'numerical experiments' conducted by Kim, Moin & Moser (1987) and Eggels *et al.* (1994) using DNS in turbulent channels and pipes, respectively, allowed us to determine that well-suited numerical simulations of the Navier–Stokes equations produce results comparable to experiments. Moreover, they have the advantage that different quantities of the flow fields can be sampled at any point of the computational domain (Jiménez 2003).

In this context, Chung (2005) investigated the DNS results of an accelerating turbulent channel undergoing a sudden change in pressure gradient at low Reynolds numbers. Their results revealed that during the ramp-up produced in the flow rate, there exists a delay in the turbulence response, consistent with previous experimental studies (Maruyama *et al.* 1976; Kurokawa & Morikawa 1986; He & Jackson 2000). Afterwards, Jung & Chung (2012) used large-eddy simulations to replicate the ramp-up flows by He & Jackson (2000). Their results confirmed that the turbulence development in a temporally accelerating pipe flow follows three stages: weak-time dependent, strong-time dependent and pseudosteady. Nonetheless, the mechanisms producing these three stages are the same as the ones indicated in the former experimental investigation.

In a similar vein, He & Seddighi (2013) performed a DNS simulation of an accelerating turbulent channel flow following a stepwise increase in the flow rate and carefully analysed several flow statistics. The results from that study revealed that the time response of the mean skin friction coefficient (C_f) followed a bypass-transition-like development. Based on the behaviour of C_f, it was suggested that turbulence in the flow followed three

transient stages: pretransition, transition and fully turbulent. The pretransition stage is characterised by elongated streaks in the streamwise direction and a decay in the skin friction coefficient produced mainly by a perturbation laminar boundary layer that grows and develops with time. The transitional stage starts approximately when the skin friction coefficient attains a minimum. During the transition period, turbulent spots appear, and they grow and merge, producing 'new' turbulence; thereby, the skin friction coefficient recovers and overshoots the final steady state at the end of this period. During the fully turbulent stage, turbulence finishes its development until the flow is thoroughly established, C_f remains nearly steady, and the universal laws of turbulence are reproduced at the highest Reynolds number attained.

Recently, Guerrero *et al.* (2021) performed a series of DNS of accelerating turbulent pipe flows between two steady Reynolds numbers. The analysis of the mean flow dynamics of those DNS time series complemented previous investigations. It revealed that a turbulent pipe flow following a rapid and linear acceleration exhibits four unambiguous stages: (I) inertial, a rapid increase in viscous forces and frozen turbulence behaviour; (II) pretransition, a weak turbulence response in the near-wall region with a simultaneous fast reduction in the viscous forces; (III) transition, a proportional increase in viscous and turbulent forces at the inner region; and (IV) core-relaxation, a slow propagation of turbulence from the wall towards the wake region. The four-stage point of view in accelerating pipe and decelerating flow has been well accepted in the community, and it has also proven to provide a suitable foundation for the study of periodic (i.e. pulsatile) transient flows (see Liu *et al.* 2024; Taylor & Seddighi 2024). Moreover, based on the Fukagata–Iwamoto–Kasagi (FIK) identity developed by Fukagata, Iwamoto & Kasagi (2002), Guerrero and coworkers derived several alternative expressions suitable to decompose the skin friction coefficient of an unsteady pipe flow into its dynamic contributions in integral form (Guerrero *et al.* 2021, 2022, 2023). This decomposition helps determine how the different terms of the mean momentum balance influence the mean wall shear stress as a function of time.

1.2. *Motivation*

The recent textbook by Ciofalo (2022), in the context of unsteady turbulent flows (pulsating and non-periodic accelerating/decelerating flows), states, '[. . .] The influence of temporal acceleration on turbulence is a different and more subtle issue, which (in the author's opinion) has not found in the literature a really satisfactory treatment so far. [. . .]'. Notably, the extant literature has provided a suitable understanding of the mean flow characteristics in rapidly accelerating flows. Indeed, it is well established in the current literature that a perturbation boundary layer develops during the early flow excursion. Additionally, there is an understanding of how the components of the Reynolds stress tensor and viscous and turbulent forces vary across different transient periods in a mean sense. On the other hand, the structural features of accelerating flows are less well understood. It is now recognised that low-speed streaks in the buffer region become elongated, and wall shear stress is reduced during the pretransitional period, followed by a retransition to a higher turbulent state. However, from a structural point of view, the roles of large-scale motions (LSM) and small-scale motions (SSM) during the transient flow development and their impact on frictional drag across the entire flow domain remain unclear.

This study investigates several turbulence statistics of accelerating turbulent pipe flow to address these gaps, focusing on analysing the spectrograms of different flow quantities. Thus, this paper aims to shed light on how LSM and SSM respond across the transient

process undergone by an accelerating turbulent pipe flow subjected to a rapid and finite ramp-up acceleration. The premultiplied cospectra of the Reynolds shear stress is investigated, and high/low-pass Fourier filters have been utilised to investigate the role of LSM and SSM in the Reynolds shear stress transient response. The premultiplied cospectra of velocity–vorticity correlations are utilised to understand the effects of LSM and SSM on turbulence decay and retransition in linearly accelerating turbulent pipe flow has also been examined. Inspired by previous studies (Guala *et al.* 2006; Wu, Baltzer & Adrian 2012; Chin *et al.* 2014), we analysed the wall-normal gradient of the Reynolds shear stress cospectra, known as the net-force spectra.

Finally, we use the FIK identity to explore the influence of large- and small-scale flow dynamics on the temporal evolution of frictional drag. By addressing these essential aspects, we aim to contribute to a deeper understanding of turbulence dynamics in accelerating flows, with potential implications for flow control and technological applications.

2. Numerical details

Direct numerical simulation data sets of an accelerating turbulent pipe flow from Guerrero *et al.* (2021) have been used in this investigation. The numerical simulations used the spectral Navier–Stokes solver Nek5000 (Fischer, Lottes & Kerkemeier 2019). It should be noted that the flow domain has a streamwise length $L = 8\pi R$ to obtain converging statistics, as suggested by Chin *et al.* (2010). Moreover, the pipe has periodic boundary conditions at both ends. The Cartesian spectral grid used seventh-order Gauss–Lobato–Legendre quadrature points at each spectral element. To obtain the DNS volumetric time series, fully developed turbulent flow fields at an initial steady friction Reynolds number $Re_{\tau,0} \approx 500$ from Guerrero, Lambert & Chin (2020) are linearly accelerated in dimensionless ramp-up time $\Delta t^{+0} = 11.8$ by increasing their flow rate until they attain a value $Re_{\tau,1} \approx 670$. Subsequently, the flow remains at a constant flow rate until it attains a fully developed state. The volumetric time series results have been spectrally interpolated from the Cartesian spectral grid to a cylindrical mesh for turbulence statistical analyses due to the nature of the pipe flow. Therefore, this study has adopted a cylindrical coordinate system where r, θ and z are the radial, azimuthal and streamwise directions, respectively. The wall-normal direction is denoted as $y = R - r$.

The computational grid has been discretised using Chebyshev polynomials in the wall-normal direction. Also, it is equally spaced in the two other homogeneous directions of the periodic pipe, and its resolution is $\Delta z^{+1} = 7.4$, $R\Delta\theta^{+1} = 6.3$, $y_{wall}^{+1} = 0.05$ and $y_{core}^{+1} = 7.5$. Note that the superscripts '+0' and '+1' denote normalisation in wall units at the initial and final steady Reynolds numbers, respectively. Indeed, the mesh used in the present study was designed to have a suitable resolution at the highest Reynolds number attained. The resolved velocity vector fields contain three orthogonal scalar components $U_r = -U_y$, U_θ and U_z whose fluctuating components are $u_r = -u_y$, u_θ and u_z, respectively. It should be noted that the present data sets have been validated with the results by He & Seddighi (2013). The reader is directed to Guerrero *et al.* (2021) for further details of the simulation and its validation.

3. Reynolds shear stress decomposition and its impact on the skin friction

3.1. *Mean velocity profile*

The time evolution of the mean velocity profile of the accelerating turbulent pipe flow analysed in this investigation is depicted in figure 1. All the velocity profiles have been
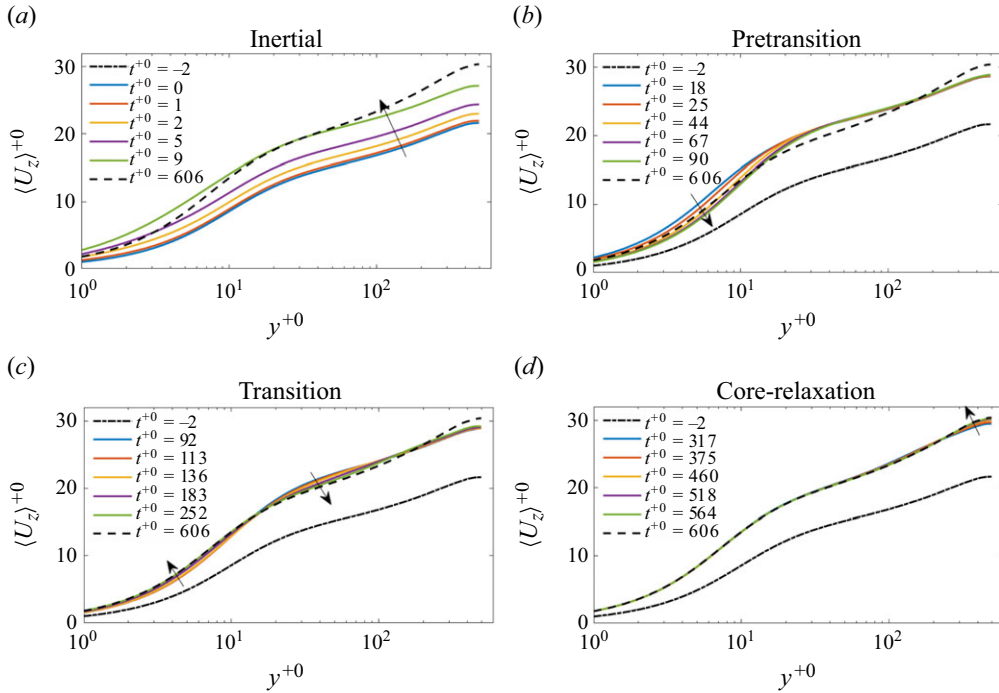
Figure 1. Time dependence of the mean velocity profile normalised with the initial friction velocity u_τ^{+0} during the (*a*) inertial, (*b*) pretransition, (*c*) transition and (*d*) core-relaxation stages. The dash–dot line $(-\cdot-\cdot-)$ represents the initial steady state, and the dashed line $(---)$ stands for the final steady state. The arrows show a time increase.

normalised with the friction velocity of the initial turbulent base flow (u_τ^{+0}) at $Re_\tau \approx 500$. In figure 1(*a*), corresponding to the inertial period, the mean velocity profile is shifted upwards from the buffer region up to the pipe centreline $(y^{+0} > 10)$. However, the viscous sublayer $(y^{+0} \leqslant 5)$ does not exhibit the well-known linear behaviour characteristic of wall-bounded canonical flows (i.e. $U^+ = y^+$) due to the momentary increase in the pressure gradient. Similar findings have been reported in previous studies where a perturbation boundary layer was observed during the early transient stages in accelerating channel and pipe flows (Kurokawa & Morikawa 1986; He & Seddighi 2015; He *et al.* 2016; Joel Sundstrom & Cervantes 2017). In essence, during the inertial stage, turbulence remains nearly frozen (Maruyama *et al.* 1976), and the mean velocity profile is represented by the imposition of a plug-like potential flow added to the mean velocity profile of the turbulent base flow at $t^{+0} = 0$, resulting in high velocity gradients at the near-wall region and a rapid nonlinear increase in the wall-shear stress (Guerrero *et al.* 2021).

Moving to the second stage, pretransition (figure 1*b*), a reduction in the velocity magnitude at the near-wall region $(y^{+0} \lesssim 10)$ is observed. Notably, within this region and at the end of the pretransition, the mean velocity profile undershoots the values of its final steady state (dashed lines). This indicates that the perturbation boundary layer develops and grows across this period, leading to a reduction in the near-wall mean velocity gradient. Thus, the mean wall shear stress and the mean skin friction coefficient decay drastically. No significant changes are observed in the mean velocity profile in the overlap and outer flow regions. This implies that the pretransitional period is related to drastic changes in the flow kinematics and dynamics of the inner flow region (He & Seddighi 2013, 2015).

The transition period shown in figure 1(*c*) reveals a recovery in the mean profile at $y^{+0} < 15$ until it settles close to its final steady state. During this stage, turbulent spots, regions of intense localised turbulence, grow and merge, giving rise to 'new' turbulence (He & Seddighi 2013). Thus, the wall-normal gradient of the Reynolds shear stress, also known as turbulent inertia (TI), increases and accelerates the mean flow close to the wall, thereby increasing the velocity gradient, which leads to a recovery in the skin friction coefficient. Within the buffer and overlap regions ($15 \lesssim y^{+0} \lesssim 200$), the mean velocity profile moves downwards and is reshaped closer to its final steady state. In contrast, the core region of the flow remains relatively unchanged.

Finally, figure 1(*d*) illustrates the behaviour during the core-relaxation stage, where the mean velocity profile has converged from the wall up to $y^{+0} < 200$. In contrast, the outer flow region ($200 \lesssim y^{+0} \lesssim 500$) is shifted upwards and finally settles at its final steady state. Note that although the core region does not seem to occupy a significant proportion of the pipe due to the semilogarithmic scale of the plot, the results show that more than 50 % of the flow domain in the wall-normal direction is not fully established at the end of the transitional period. This implies that the core-relaxation stage requires large time scales for 'new turbulence' to propagate from the wall towards the pipe centreline. Therefore, the core region requires a long period to attain its final steady state.

It is worth noting that although the primary aim of this investigation is not to examine the mean profile, a brief analysis of its behaviour is required to understand further how large- and small-scale turbulent structures exert influence on the mean velocity profile during the different transient periods, as will be shown in the following sections.

3.2. *Time dependence of the Reynolds shear stress*

The Reynolds shear stress, decomposed into its large- and small-scale contributions, can be investigated to understand how LSM and SSM contribute during the transient development of the accelerating turbulent pipe flow. The cospectra of the Reynolds shear stress is defined as $\phi_{u_r u_z} = \mathbb{R}[(\hat{u_r}^*)(\hat{u_z})]$, where $\hat{u_r}$ and $\hat{u_z}$ are the Fourier transforms of the radial and streamwise velocity fluctuations, respectively, and $\mathbb{R}$ denotes the real part of the product. The small- and large-scale components of the Reynolds shear stress can then be computed as $\langle u_r u_z \rangle_{SS} = \int_0^{\lambda_{th}} \phi_{u_r u_z}(\lambda_z) \mathrm{d}\lambda_z$ and $\langle u_r u_z \rangle_{LS} = \int_{\lambda_{th}}^{\infty} \phi_{u_r u_z}(\lambda_z) \mathrm{d}\lambda_z$, respectively, where λ_{th} is a wavelength threshold that demarcates the separation of small and large scales. This threshold is chosen based on the definitions by Guala *et al.* (2006), Hutchins & Marusic (2007) and Balakumar & Adrian (2007), who explain that LSM typically have wavelengths in the range of two to three pipe radii and very large-scale motions (VLSM) have wavelengths greater than three pipe radii. Moreover, Ahn *et al.* (2015) explains that at the outer flow region (i.e. $y/R \geqslant 0.1$), the threshold for SSM occurs at wavelengths where $\lambda/R \leqslant 2$.

Figure 2 depicts the Reynolds shear stress $\langle u_r u_z \rangle^{+0}$ decomposed into the large- and small-scale components using a wavelength threshold $\lambda_{th} \approx 2R$ (i.e. $\lambda_{th}^{+0} \approx 1000$). This decomposition was performed using a high/low pass Fourier filter similar to Chin *et al.* (2014). The results show that during the inertial stage (figure 2*a*), the turbulence associated with LSM and SSM is completely frozen. This reveals that the pre-existing turbulence in the base flow does not undergo significant changes during the inertial period, thus confirming the 'frozen turbulence' occurring during this stage (Maruyama *et al.* 1976).

Throughout the pretransitional stage (figure 2*b*) it is observed a dominant response in the large-scale turbulent motions, providing further evidence of the streak elongation (He & Seddighi 2013) and possibly a stretching of streamwise vortices produced by the high strain
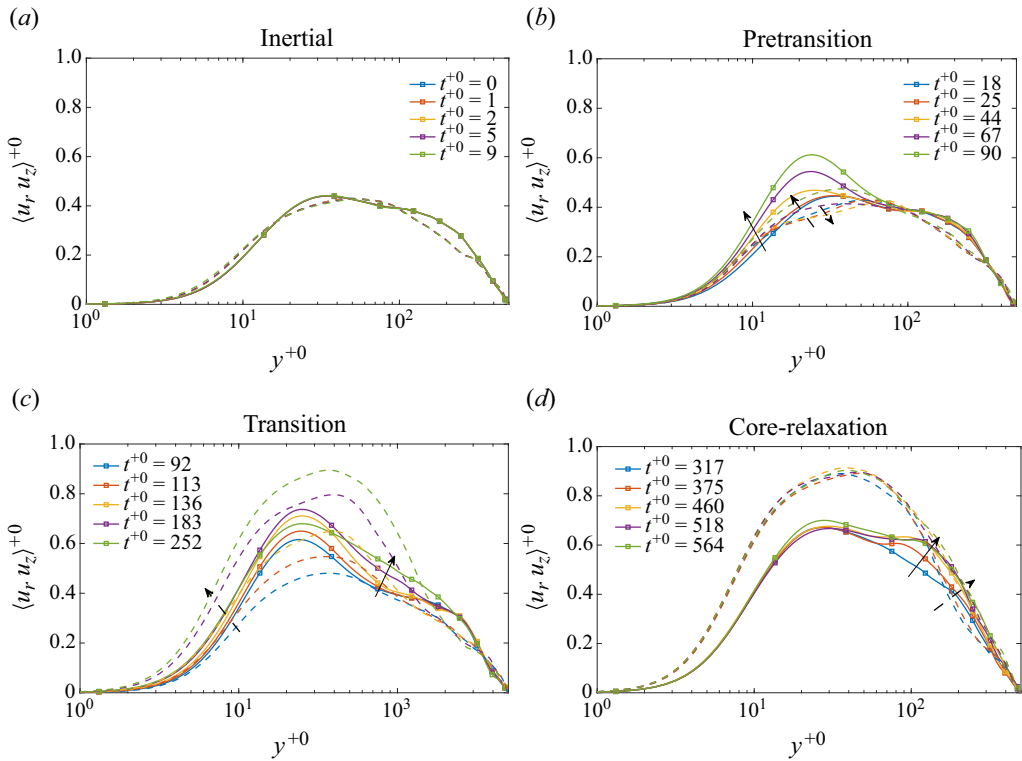
Figure 2. Time dependence of the large-scale (solid) and small-scale (dashed) components of the Reynolds shear stress during (*a*) the inertial, (*b*) pretransition, (*c*) transition and (*d*) core-relaxation stages. The time increase is represented by a solid arrow for the LSM and dashed for the SSM.

produced by perturbation boundary layer generated during the inertial period. Note that this perturbation boundary layer grows and develops throughout the pretransition stage. It is also interesting to note that there is a decay in the contribution of the small-scale structures into the Reynolds shear stress between $18 \lesssim t^{+0} \lesssim 44$, implying a laminarescent trend in small-scale turbulence occurring during the early pretransition. A further analysis of the small-scale decay mechanism is presented in § 4.2.

The decomposition of LSM and SSM of $\langle u_r u_z \rangle^{+0}$ across the transitional period is depicted in figure 2(*c*). Growth in both LSM and SSM turbulence is observed. However, a careful examination shows that within the inner region of the flow $y^{+0} \lesssim 100$, the SSM turbulence (dashed lines) develops faster. It should be noted that within the core region of the flow, both SSM and LSM turbulence remain nearly unchanged. Therefore, further evidence is provided that 'new' turbulence, produced at the wall, requires significant time scales to propagate towards the pipe centreline.

Finally, figure 2(*d*) exhibits the results computed during the core-relaxation stage. Throughout this period, the LSM and SSM contributions are nearly frozen at the near-wall region, which shows that the near-wall region is nearly established. Large-scale contributions present mild growth in the buffer and overlap regions ($15 \lesssim y^{+0} \lesssim 100$). Small scales present a fluctuating behaviour at this same location, presenting a slight growth between $40 \leqslant y^{+0} \leqslant 100$. At the outer flow region $100 \lesssim y^{+0} \lesssim 500$, both large- and small-scales reveal a significant growth.
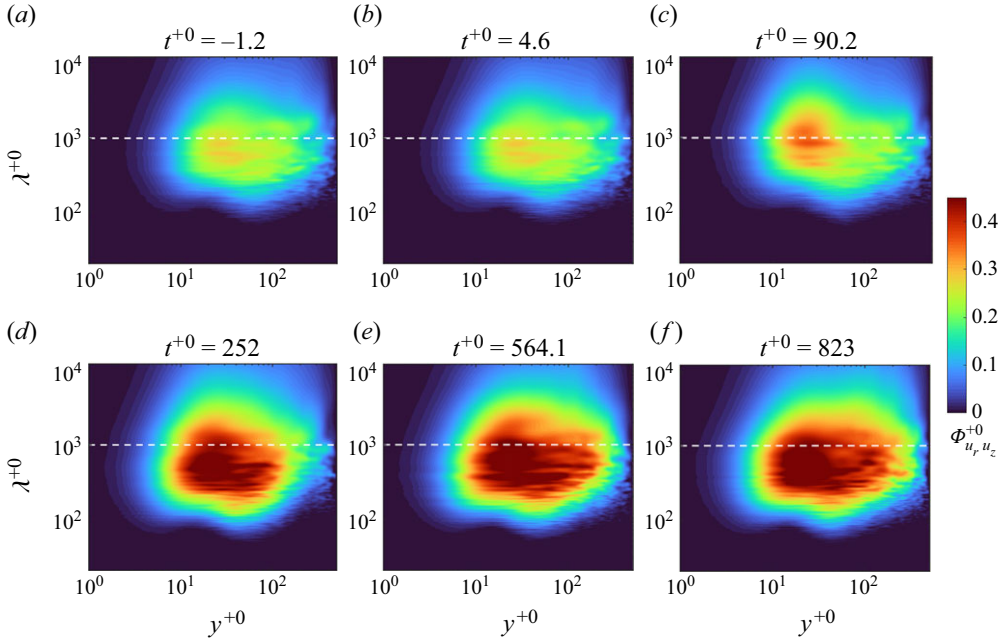
Figure 3. Temporal evolution of the Reynolds shear stress premultiplied cospectra $\Phi_{u_r u_z}^{+0}$ throughout the different stages undergone by the flow: (*a*) initial steady-state; (*b*) inertial; (*c*) pretransition; (*d*) transition; (*e*) core-relaxation; (*f*) final steady-state. The white dashed line represents the threshold used to decompose the LSM and the SSM.

To further understand how large- and small-scales contribute to the energy growth of the Reynolds shear stress, the premultiplied cospectra of $\langle u_r u_z \rangle$ are analysed in the following section.

3.3. *Energy growth in the Reynolds shear stress*

Figure 3 depicts the temporal evolution of the Reynolds shear stress' premultiplied wavenumber energy cospectra $\Phi_{u_r u_z}^{+0} = k_z \phi_{u_r u_z}^{+0}$ during a particular time location at the initial steady-state (figure 3*a*), the four transient stages (figure 3*b−e*) and the final steady-state (figure 3*f*). The premultiplied streamwise energy cospectra allow the measurment of the turbulence energy contained in different wavelengths in the streamwise direction.

The Reynolds shear stress premultiplied cospectra exhibited in figure 3(*a*) show that the inner peak at the initial steady-state at $Re_\tau \approx 500$ is located at $y^{+0} \approx 30$ and $\lambda^{+0} \approx 700$, showing consistency with previous studies in steady turbulent pipe flow (Chin *et al.* 2014; Ahn, Lee & Sung 2017). Moreover, it is noticed that $\Phi_{u_r u_z}^{+0}$ in figures 3(*a*) and 3(*b*) do not exhibit any significant changes between the base flow and the inertial steady-state.

Throughout the pretransitional period (figure 3*c*), it is noted that $\Phi_{u_r u_z}$ exhibits an energy growth in turbulent scales ranging from $600 \lesssim \lambda^{+0} \lesssim 8000$ located at the buffer region. Nonetheless, the overlap and outer flow regions do not show any relevant changes.

The transition stage, shown in figure 3(*d*) exhibits growth mainly in SSM (i.e. $\lambda^{+0} < 1000$) at a wall position of $5 \lesssim y^{+0} \lesssim 100$. This reveals that 'new' turbulence produced at the end of the pretransitional stage, resulting from the instability growth explained by He & Seddighi (2013) in accelerating channel flow, mainly produces small-scale turbulence propagated by different transport phenomena such as advection and diffusion across the
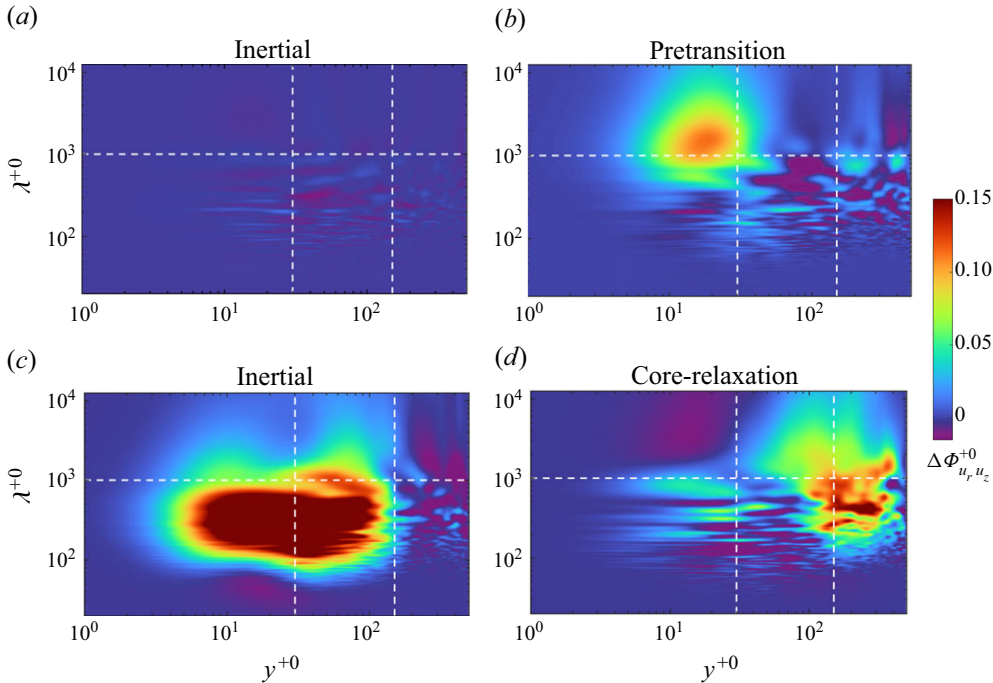
Figure 4. Energy growth in the Reynolds shear stress cospectra throughout the four transitional stages undergone by an accelerating flow. The energy growth at each stage were obtained by subtracting two consecutive spectrograms from figure 3($a-e$). The vertical dashed lines are located at $y^{+0} = 40$ and $y^{+0} = 200$, and the horizontal dashed line is located at $\lambda^{+0} = 1000$ ($\lambda/R = 2$).

inner flow region. Nonetheless, the wake region does not exhibit significant changes in the spectrogram compared with the inertial and pretransition periods (figure 3b,c).

The Reynolds stress spectrogram of the core-relaxation period is shown in figure 3(e). Herein, it is noted that within $y^{+0} \lesssim 40$, the spectrogram does not exhibit significant changes in all the range of scales. This implies that the flow has been established at the near-wall and buffer regions. Nonetheless, an energy growth of turbulence energy at the outer flow region is noted.

It should be noted that the cospectra alone does not provide an accurate qualitative and quantitative indication of energy growth. Thus, the difference in two consecutive spectrograms (i.e. $\Delta\Phi^{+0}_{u_r u_z} = \Phi^{+0}_{u_r u_z}(t + \Delta t) - \Phi^{+0}_{u_r u_z}(t)$) provides a clearer picture of what scales of motion gain energy throughout the transient process. Figure 4 exhibits the results of that subtraction. For instance, figure 4(a) is the result of subtracting $\Phi^{+0}_{u_r u_z}(t^{+0} = 4.6) - \Phi^{+0}_{u_r u_z}(t^{+0} = -1.2)$ (i.e. figure 3b – figure 3a). Moreover, it should be noted that the spectrogram has been subdivided into six quadrants to understand better the regions and the length scales at which the energy growth occurs. In that context, the two vertical dashed lines subdivide the near-wall ($y^{+0} < 30$), overlap ($30 \lesssim y^{+0} \lesssim 200$) and wake ($y^{+0} > 200$) regions of the flow. Similarly, the horizontal line subdivides the scale ranges into SSM ($\lambda^{+0} \leqslant 1000$) and LSM, where $\lambda^{+0} > 1000$ (i.e. $\lambda/R > 2$).

The results observed in figure 4(a) show that while the mean kinetic energy of the fluid increases owing to the acceleration imposed on the turbulent base flow, the turbulent energy does not exhibit any significant changes throughout the pipe domain due to the delay in the turbulence response characteristic of the inertial period. These results agree with the 'frozen' turbulence observed during the early flow excursion observed in

previous studies (Maruyama *et al.* 1976; He & Jackson 2000). Figure 4(*b*) shows that during the pretransition, LSM exhibit considerable energy growth at the buffer region, providing further evidence of the formation of elongated streaks at the near-wall region in accelerated wall-bounded internal flows. As explained in the literature, the streamwise velocity streaks at the buffer region elongate (He *et al.* 2016), and the mean streamwise normal stress $\langle u_z u_z \rangle$ grows locally at this region owing to the stretching of the near-wall quasistreamwise vortices, whose enstrophy increases to preserve the angular momentum (Guerrero *et al.* 2021).

The energy growth in the Reynolds shear stress throughout the transition period is observed in figure 4(*c*). This figure reveals that most of the energy growth and the turbulence production at the inner region of the flow (i.e. $y^{+0} < 100$) occurs during the transition stage. During this period, small-scale structures of size $100 \lesssim \lambda^{+0} \lesssim 1000$ are generated, contributing to the generation of 'new' turbulence. Moreover, a small (purple) region of energy decay is observed between $10 \lesssim y^{+0} \lesssim 30$ and $\lambda^{+0} < 80$, revealing the occurrence of a mild energy decline in small-scale turbulence at the buffer region during the transition period.

Finally, figure 4(*d*) reveals substantial growth in the energy density at the wake region of the flow within the small- and large-scale spectrum $300 \lesssim y^{+0} \lesssim 10^4$. Also, it is noted that there is mild energy growth at the near-wall region during the core relaxation period. It is also interesting to notice the presence of a turbulent energy decay region located between $5 \lesssim y^{+0} \lesssim 30$ and $4 \lesssim \lambda/R \lesssim 8\pi$, evidencing a slight energy decay in LMS and VLMS during the core-relaxation period. This energy deficit, could most likely be attributed to an energy transport occurring from the buffer towards the overlap and outer flow regions, consistent with the radial propagation of turbulence observed by Maruyama *et al.* (1976).

3.4. *Contribution of LSM and SSM into the wall friction*

An exact expression that aids in further understanding the different contributions of the terms in the mean momentum balance equation of an unsteady turbulent flow to the skin friction coefficient was developed by Fukagata *et al.* (2002). This expression, commonly known as the FIK identity, has been applied to the numerical dataset used in this investigation following the alternative expression derived by Guerrero *et al.* (2021) for unsteady pipe flow. However, this expression was multiplied by $0.5\rho[U_b(t)]^2$ to express the frictional drag in terms of the wall shear stress (τ_w) rather than the skin friction coefficient. The wall shear stress decomposition is shown as follows:

$$\tau_w = \underbrace{\frac{4\rho\nu U_b}{R}}_{\tau_w^\delta} + \underbrace{8\rho U_b^2 \int_0^1 2r^* \langle u_r u_z \rangle^* \, r^* \mathrm{d}r^*}_{\tau_w^T}$$
$$\underbrace{- 8\rho U_b^2 \int_0^1 \left((r^*)^2 - 1 \right) \left(\frac{1}{r^*} \frac{\partial (r^*\tau^*)}{\partial r^*} - \frac{2}{R} \int_0^1 \frac{1}{r^*} \frac{\partial (r^*\tau^*)}{\partial r^*} r^* \mathrm{d}r^* \right) r^* \mathrm{d}r^*}_{\tau_w^U}. \quad (3.1)$$

The contributions to the wall shear stress in (3.1) can be understood as follows. The first term on the right-hand side (τ_w^δ) is associated with the Fanning friction coefficient and represents the laminar contributions to the flow. The second term (τ_w^T) directly correlates with the Reynolds shear stress, representing turbulent effects on wall friction. The last term on the right-hand side of (3.1), τ_w^U accounts for the unsteady contributions to the wall shear stress. Note that at the initial steady turbulent base flow and once the flow attains the
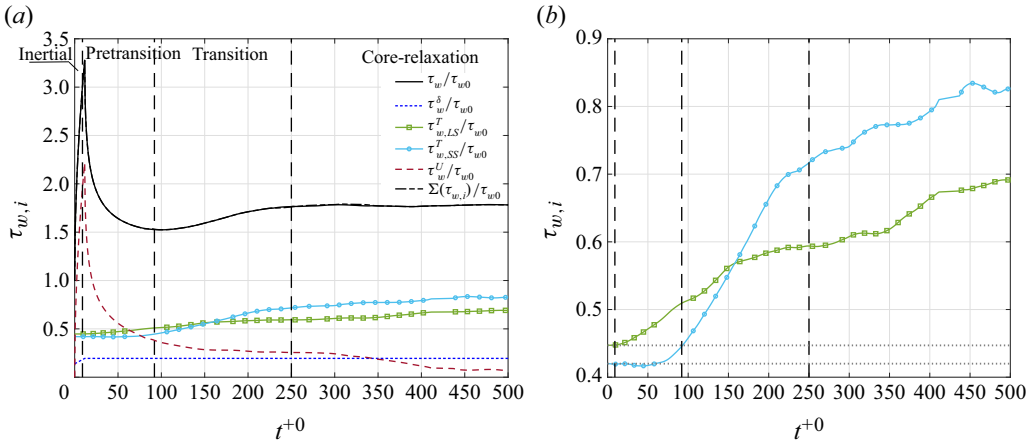
Figure 5. (a) The FIK decomposition of the wall shear stress of an accelerating turbulent pipe flow. (b) Zoomed-in view of the turbulent term decomposed into the large-scale ($\tau_{w,LS}^T$) and small-scale contributions ($\tau_{w,SS}^T$). The vertical dashed aim to distinguish the four transient stages described in this study.

final steady-state, $\tau_w^U = 0$. For a further explanation into the derivation of this identity the reader is directed to Fukagata *et al.* (2022) and Guerrero *et al.* (2021, 2022).

Note that all the physical variables in (3.1) have been normalised by $2U_b$ and the pipe radius R (e.g. the mean streamwise velocity $U_z(r,t)$ has been normalised as $U_z^* = U_z/(2U_b)$, the spatial domain in the radial direction was normalised as $r^* = r/R$ and the time domain was normalised as $t^* = t/(2U_b/R)$) as explained by Fukagata *et al.* (2002). The symbol τ^* stands for the total normalised shear stress, which adds the Reynolds and the viscous shear stresses (i.e. $\tau^* = \langle u_r u_z \rangle^* - 1/Re_b \langle dU_z/dr \rangle^*$).

As previously described, the Reynolds shear stress can be decomposed using a high/low pass Fourier filter as $\langle u_r u_z \rangle = \langle u_r u_z \rangle_{LS} + \langle u_r u_z \rangle_{SS}$, where the subscripts LS and SS denote the large- and small-scale contributions, respectively (see figure 2). Consequently, τ_w^T can be further divided into large- and small-scale turbulent contributions to the frictional drag. With this consideration, the decomposition of the wall shear stress can be expressed as follows:

$$
\tau_w = \underbrace{\frac{4\rho\nu U_b}{R}}_{\tau_w^\delta} + \underbrace{8\rho U_b^2 \int_0^1 2r^* \langle u_r u_z \rangle_{LS}^* r^* dr^*}_{\tau_{w,LS}^T} + \underbrace{8\rho U_b^2 \int_0^1 2r^* \langle u_r u_z \rangle_{SS}^* r^* dr^*}_{\tau_{w,SS}^T}
$$
$$
\underbrace{- 8\rho U_b^2 \int_0^1 \left((r^*)^2 - 1 \right) \left(\frac{1}{r^*} \frac{\partial(r^* \tau^*)}{\partial r^*} - \frac{2}{R} \int_0^1 \frac{1}{r^*} \frac{\partial(r^* \tau^*)}{\partial r^*} r^* dr^* \right) r^* dr^*}_{\tau_w^U}. \quad (3.2)
$$

Equation (3.2) has been applied to the present DNS data sets. Firstly, it should be noted that the summation of all contributions ($\Sigma \tau_w, i$) collapses with the transient mean wall shear stress τ_w as shown in figure 5(a), providing confidence in the results obtained. Moreover, the results exhibited in figure 5(a) reveal that the LSM and SSM components of the turbulent term exhibit a substantially different response, especially during the inertial and the pretransition stages. The turbulent contribution associated with the small-scale components $\tau_{w,SS}^T$ seems nearly unchanged during the inertial and the pretransitional

periods. However, the large-scale turbulent contribution $\tau_{w,LS}^T$ only exhibits a frozen be-haviour during the first stage and undergoes linear growth during the pretransition period.

A zoomed-in view of $\tau_{w,LS}^T$ and $\tau_{w,SS}^T$ is provided in figure 5(*b*) to understand better the contributions of the large- and small-scale contributions of the Reynolds shear stress into τ_w. Firstly, it is noted that along the inertial and pretransition stages, the large-scale turbulent contributions (green line) seem to be dominant in producing frictional drag. Herein, the small-scale contribution, $\tau_{w,SS}^T$, experiences a mild decay at $20 \lesssim t^{+0} \lesssim 60$, thereby suggesting a laminarescent trend of small-scale turbulence during the pretransitional stage. Nonetheless, large-scale turbulent motions increase their contributions linearly to τ_w across the pretransition stage.

Throughout the transition stage, the small-scale contributions grow with a higher slope, and by the late transitional stage, SSM with $\lambda < 2R$ become the most significant contrib-utors of frictional drag. These results imply that small-scale turbulent motions produce the highest energy dissipation throughout the transition stage, increasing frictional drag. Finally, along the core-relaxation period, there is a mild growth in the contributions of both large- and small-scale turbulence. Nonetheless, the small-scale turbulent motions remain the dominant contributors until the flow establishes and attains the final steady state.

The unsteady τ_w^U and the laminar τ_w^δ terms of the present wall-shear stress decomposition exhibit the same behaviour explained in Guerrero *et al.* (2021, 2022).

4. Turbulent inertia: decomposition and spectral analysis

The mean momentum balance of an unsteady turbulent flow in cylindrical coordinates is as folllows: The term on the left-hand side is the acceleration or inertia force. The first term on the right-hand side is the pressure gradient. The second term on the right-hand side is related to the viscous shear stress and represents the viscous force. Finally, the last term of (4.1) is the gradient of the Reynolds shear stress, also known as turbulent inertia (TI) or turbulent force.

The TI, $1/r\partial/\partial r(-r\langle u_r u_z\rangle)$, can be physically understood as the mean transport of turbulent momentum (Adrian 2007). It should also be noted that the TI is zero at the wall, and acts as a source term at the near-wall region before the Reynolds shear stress attains a peak value (i.e. at a wall-normal location y_p) and has negative values from y_p up to the pipe centreline. This indicates that the TI acts as a source term that accelerates the mean flow at the near wall region (below y_p) and retards it at the outer region, producing the flatter mean velocity profile, characteristic of turbulent wall-bounded flows.

$$\underbrace{\frac{\partial \langle U_z\rangle}{\partial t}}_{IF} = \underbrace{-\frac{1}{\rho}\frac{\mathrm{d}p}{\mathrm{d}z}}_{PG} + \underbrace{\frac{1}{r}\frac{\partial}{\partial r}\left(r\nu\frac{\partial \langle U_z\rangle}{\partial r}\right)}_{VF} + \underbrace{\frac{1}{r}\frac{\partial}{\partial r}\left(-r\langle u_r u_z\rangle\right)}_{TI}. \quad (4.1)$$

The time evolution in the TI and the viscous force for the accelerating turbulent case used in this investigation has been previously analysed (Guerrero *et al.* 2021). Instead, this study focuses on analysing the transient contributions of TI by decomposing it in terms of the velocity–vorticity correlations and as a function of the gradient of the premultiplied Reynolds shear stress cospectra, also known as the net-force spectra (Guala *et al.* 2006).

4.1. *Velocity–vorticity correlations*

The TI (Reynolds stress gradient) can be represented in terms of the velocity–vorticity correlations as explained by Klewicki (1989, 2013). The Reynolds stress gradient in a turbulent pipe flow can be decomposed as

$$\frac{1}{r}\frac{\partial}{\partial r}\left(-r\left\langle u_r u_z\right\rangle\right) = \left\langle u_r\omega_\theta\right\rangle - \left\langle u_\theta\omega_r\right\rangle. \tag{4.2}$$

Equation (4.2) establishes a direct relationship between vorticity transport and the Reynolds shear stress. In turbulent pipe flows, the mean velocity gradient, $\mathrm{d}U_z/\mathrm{d}y$, provides the largest contribution to the azimuthal vorticity (ω_θ). Consequently, the viscous stress can be approximated as $\mu\mathrm{d}U_z/\mathrm{d}y \approx -\mu\omega_\theta$ (Brown, Lee & Moser 2015). This approximation highlights how TI transfers viscous stress to the Reynolds shear stress (Brown *et al.* 2015, 2020; Kumar, Meneveau & Eyink 2023).

Following the same lines, Morrill-Winter & Klewicki (2013) and Klewicki (2013) explained that the $\langle u_r\omega_\theta\rangle$ correlation is related to the wall-normal transport of azimuthal vorticity, also known as vorticity advection or vorticity dispersion. On the other hand, the $\langle u_\theta\omega_r\rangle$ term is associated with a vorticity stretching body force related to the change of scale of the vortical motions. Indeed, the investigation by Klewicki (1989, 2013) explains that $\langle u_\theta\omega_r\rangle$ is associated with a vorticity stretching and reorientation process.

The velocity–vorticity correlations of the present accelerating pipe flow DNS data sets are depicted in figure 6. The results exhibited in figure 6(*a*) show that throughout the inertial stage, there is a nearly unchanged behaviour in both $\langle u_r\omega_\theta\rangle^{+0}$ and $\langle -u_\theta\omega_r\rangle^{+0}$, denoted by solid and dashed lines, respectively. This is consistent with the 'frozen' turbulent behaviour reported during the early flow acceleration, also known as the inertial period mentioned previously in §3.2. However, it is noteworthy that throughout this period, the viscous forces (not shown in the figure), which act as a momentum sink, increase in magnitude to decelerate the flow near the wall to fulfil the no-slip condition (see Guerrero *et al.* (2021), for further details).

Figure 6(*b*) shows the temporal evolution of the velocity–vorticity correlations during the pretransition. Throughout this stage, it is noted that the vorticity stretching contribution, $\langle -u_\theta\omega_r\rangle$, is a momentum source along the inner flow region ($y^{+0} \lesssim 100$). It is also observed that after the flow excursion, the vorticity stretching body force grows in energy between $1 \lesssim y^{+0} \lesssim 40$. These results are interestingly consistent with the observations by He & Jackson (2000) and Guerrero *et al.* (2021), who assert that the mild increase in the transient turbulence response observed during the pretransitional period, is related to the stretching of the pre-existing turbulent eddies, resulting from the flow acceleration, which in turn produces elongation of the streamwise velocity streaks (He & Seddighi 2013). Similarly, the $\langle u_r\omega_\theta\rangle^{+0}$ term exhibits a mild growth within the near-wall region $1 \lesssim y^{+0} \lesssim 10$. Along $10 \lesssim y^{+0} \lesssim 100$, the advective term also grows in magnitude, on the negative side, revealing that the negative contributions to TI during this period come mainly from the advective term. It should be noted that, as explained by Adrian (2007), the TI flattens and retards the mean velocity profile at the outer flow region.

Throughout the transition stage, exhibited in figure 6(*c*), substantial growth in the stretching term is observed, the largest contributor to TI at the near-wall region. This observation is coherent with the increase of 'new' turbulence along the transition stage, especially in the small-scale spectrum, as shown in the Reynolds stress cospectrum (refer back to figure 4*c*). Notably, the peak in the turbulent force moves closer to the wall as the Reynolds number increases. The advective term, $\langle u_r\omega_\theta\rangle^{+0}$, also exhibits a significant growth at the near-wall region, which, at the end of the transitional period ($t^{+0} \approx 252$), collapses with the final steady state. Nevertheless, the outer region requires more time to establish. Indeed, along $10 \lesssim y^{+0} \lesssim 150$, the advective contribution to TI attains higher magnitudes with a negative sign. This implies that throughout this transient process, the turbulent momentum transport requires a stronger contribution from the negative region in
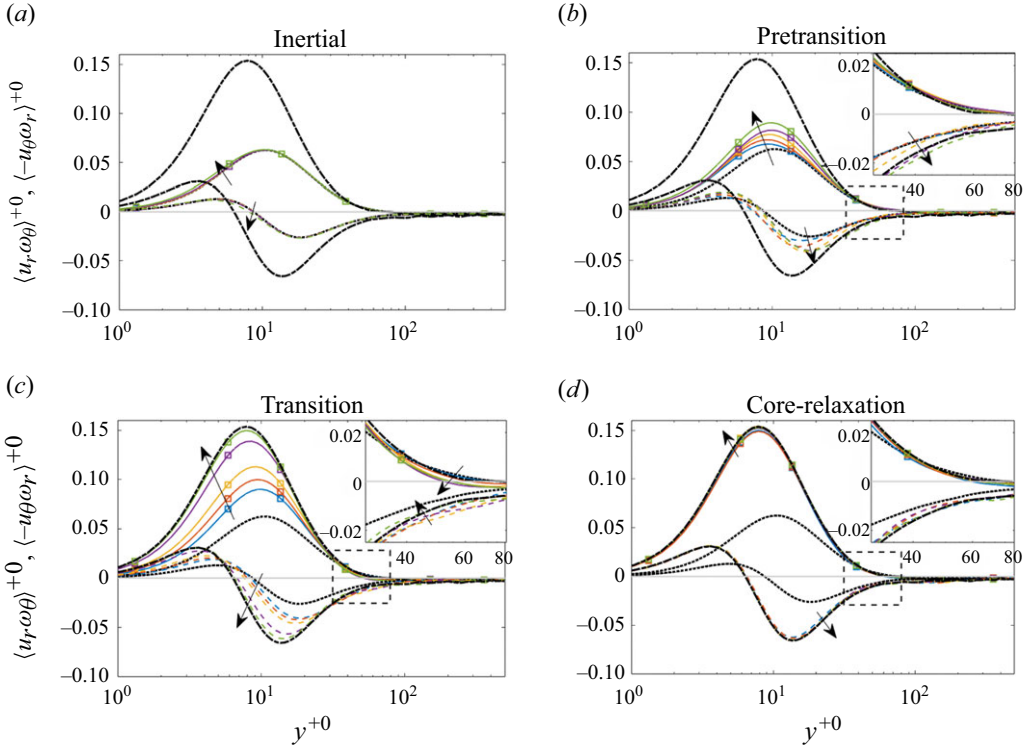
Figure 6. Time dependence of the velocity–vorticity correlations. The stretching component, $\langle -u_\theta \omega_r \rangle^{+0}$, is represented with the solid line. The advective component, $\langle u_r \omega_\theta \rangle^{+0}$ is shown with dashed lines. The velocity–vorticity correlations were computed during (*a*) the inertial, (*b*) pretransition, (*c*) transition and (*d*) core-relaxation stages. The colour legend is the same used in figure 1.

$\langle u_r \omega_\theta \rangle$ to reshape the mean velocity profile to a new turbulent state at a higher Reynolds number.

Finally, figure 6(*d*) shows that during the core-relaxation period, the stretching term exhibits a mild growth until it establishes at the near-wall region at $t^{+0} \approx 600$. On the other hand, the advective contribution to TI has already been established in the viscous sublayer $0 \lesssim y^{+0} \lesssim 5$. However, it also exhibits a mild growth in magnitude throughout the core-relaxation at $y^{+0} \gtrsim 10$, and it finally establishes near the end of the core-relaxation at $(t^{+0} \approx 600)$.

It should be noticed that as $\langle -u_\theta \omega_r \rangle^{+0}$ and $\langle u_r \omega_\theta \rangle^{+0}$ asymptote to small negative values at $y^{+0} > 100$.

A natural extension to analyse the behaviour of TI and the velocity–vorticity correlations consists in using the Fourier analysis, which is a valuable tool for further investigating the energy growth experienced by the velocity–vorticity correlations across the different transient stages. As a result, the following section analyses the spectrograms associated with the velocity–vorticity correlations.

4.1.1. *Spectral analysis of the velocity–vorticity correlations*

A useful approach for investigating the velocity–vorticity correlations was conducted by Chin *et al.* (2014). This method consists in analysing the cospectra of $\langle u_r \omega_\theta \rangle^{+0}$ and $\langle u_\theta \omega_r \rangle^{+0}$ in premultiplied form to properly quantify how different scales of motion
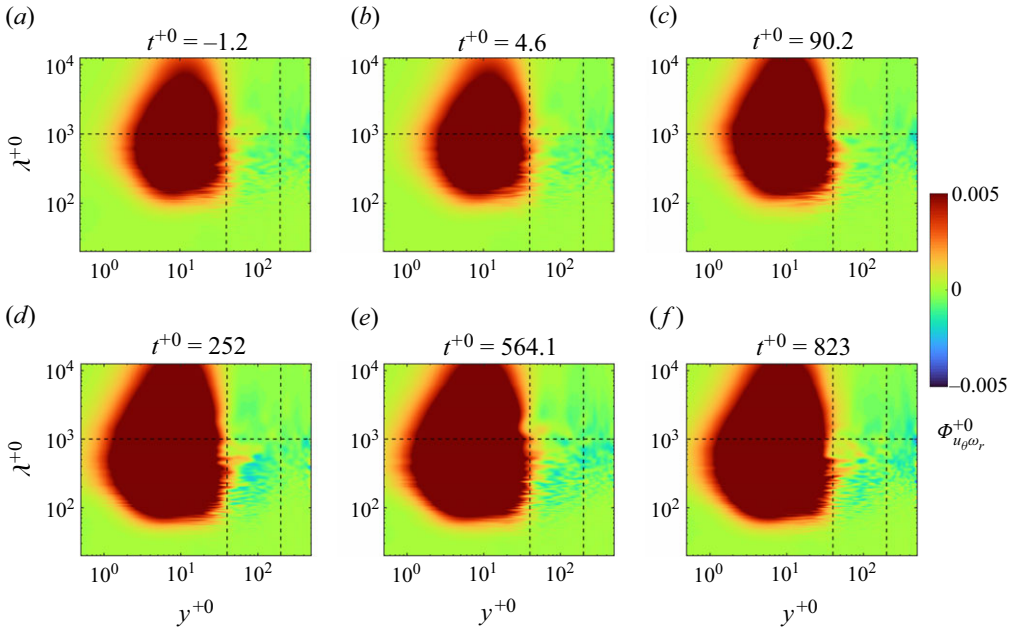
Figure 7. Temporal evolution of the vorticity stretching $\langle u_\theta \omega_r \rangle$ premultiplied cospectra $\Phi_{u_\theta \omega_r}^{+0}$ throughout the different stages undergone by the flow: (*a*) initial steady-state; (*b*) inertial; (*c*) pretransition; (*d*) transition; (*e*) core-relaxation; (*f*) final steady-state.

contribute to the energy contained in these flow quantities. The spectral decomposition of the velocity–vorticity correlations can be represented as

$$\begin{cases} \langle u_r \omega_\theta \rangle^{+0} = \int_0^\infty \Phi_{u_r \omega_\theta}^{+0} \, \mathrm{d} \log \lambda_x^{+0}, \\ \langle u_\theta \omega_r \rangle^{+0} = \int_0^\infty \Phi_{u_\theta \omega_r}^{+0} \, \mathrm{d} \log \lambda_x^{+0}, \end{cases} \tag{4.3}$$

where the variable $\Phi_{u_r \omega_\theta}^{+0} = k_z \phi_{u_r \omega_\theta}^{+0}$ represents the premultiplied cospectrum of u_r and ω_θ. Additionally, k_z is the streamwise wavenumber. The $\Phi_{u_\theta \omega_r}^{+0}$ variable follows a similar definition.

Figure 7 shows the time dependence of the stretching term cospectra, $\Phi_{u_\theta \omega_r}^{+0}$, throughout the transient period experienced by the accelerating pipe flow datasets used in this investigation. The energy contained in $\langle u_\theta \omega_r \rangle^{+0}$ does not exhibit relevant differences between the initial steady state and the inertial period (figures 7a and 7b), consistent with the 'frozen turbulence' characteristic of the inertial period. However, figure 7(*c*) evidences a relevant energy growth in the large-scale spectrum ($\lambda^{+0} \gtrsim 1000$). As time progresses, the transitional period is attained. Figure 7(*d*) shows that aside from the growth in the large-scale spectrum observed during the pretransition stage, there is a significant energy growth at the near-wall region in the small-scale range (i.e. $\lambda^{+0} < 1000$), and the appearance of a momentum sink in the small-scale spectrum at the overlap region ($40 \lesssim y^{+0} \lesssim 120$). It is noteworthy that this momentum sink. Finally, figures 7(*e*) and 7(*f*) interestingly show that during the core relaxation period, the momentum sink, which became stronger along the transient period, diffuses throughout the outer flow region.

For a more precise picture of the wall-normal location and the wavelengths contributing to the energy growth in $\langle u_\theta \omega_r \rangle^{+0}$, the difference in the consecutive spectrograms from
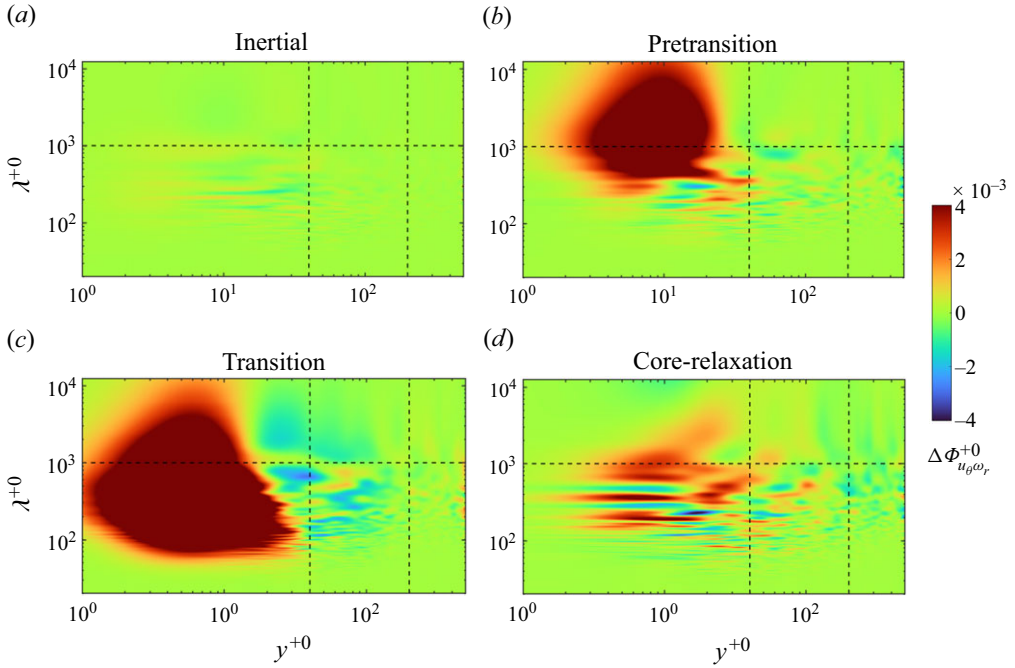
Figure 8. Energy growth in the vorticity stretching term $u_\theta \omega_r$ premultiplied cospectra ($\Delta \Phi^{+0}_{u_\theta \omega_r}$) throughout the four transitional stages undergone by an accelerating flow. The energy growth at each stage was obtained by subtracting two consecutive spectrograms from figure 7($a-e$).

figure 7(a–f) has been computed and is presented in figure 8. Throughout the inertial period, it is observed that most of the pipe domain is nearly unchanged, as observed in figure 8(a). However, a mild energy growth is noticed in the stretching term at the inner region ($y^{+0} \lesssim 50$).

Figure 8(b) shows that, throughout the pretransition, the energy growth in the stretching component occurs at the inner flow region between $2 \lesssim y^{+0} \lesssim 30$. It is important to note that the vorticity stretching body force increases substantially in scales in the range $500 \lesssim \lambda^{+0} \lesssim 12\,500$. This observation agrees with He & Seddighi (2013) and He *et al.* (2016), who observed a significant elongation of turbulent structures, specifically the streamwise velocity streaks (i.e. u_z), at the near-wall region. Nevertheless, the present analysis reveals that other flow structures, such as vortical structures, tend to increase in length and energy due to stretching and tilting in the large-scale spectrum owing to the acceleration imposed on the base flow. It is also interesting to notice that the 'footprint' in the energy growth of $\Delta \Phi^{+0}_{u_\theta \omega_r}$ throughout the pretransitional stage exhibits strong similarities with the energy growth in the Reynolds shear stress energy growth spectra $\Delta \Phi^{+0}_{u_r u_z}$ (refer back to figure 4b). It is not surprising as the $\langle u_\theta \omega_r \rangle^{+0}$ term provides the most significant contributions to the gradient of the Reynolds shear stress at the near-wall region.

During the transition stage, exhibited in figure 8(c), we noticed a growth in the vorticity stretching force at the near-wall region, mainly in the small-scale spectrum. However, a relevant growth in LSM has also been noticed. This shows a possible enstrophy growth throughout the transitional period due to stretching. Small scales also play a relevant role during this period, revealing that streaks break down and small-scale vortical structures are produced due to the 'new vorticity' generated during the flow excursion. The breakdown

1010 A37-18

process and the production of new vortical structures is a transitional process which exhibits similarities with the transition from laminar to turbulent flows (He & Seddighi 2013, 2015; Guerrero *et al.* 2021). By the end of the transitional period, it is also possible to observe energy decay in $\langle u_\theta \omega_r \rangle^{+0}$ in the buffer and the overlap regions and in both large- and small-scale wavelengths (i.e. $100 \lesssim \lambda^{+0} \lesssim 10\,000$). This is consistent with the decay observed in the behaviour of the mean stretching term as previously observed in the inset of figure 6(*c*). This implies that as the flow establishes due to the acceleration experienced by the flow during the inertial period, a momentum sink is produced within the buffer and log regions (denoted by vertical dashed lines). This is a relevant observation as regions with momentum deficit contribute to the negative values of TI, which flatten the mean velocity profile as the Reynolds number increases.

The spectral energy growth in the stretching term during the core-relaxation period is shown in figure 8(*d*). Here, there is a small energy growth in the small-scale spectrum at the near-wall region. Nevertheless, it is interesting to notice that within the buffer and the overlap regions, mild energy growth in the large-scale spectrum ($\lambda^{+0} > 1000$) positively contributes to the formation region E in the force spectra (shown later) as explained by Chin *et al.* (2014). It should be mentioned that the force spectra in the accelerating flow analysed in this study will be examined later in § 4.2.

As mentioned above, the other relevant contribution to the turbulent force comes from the advective correlation $\langle u_r \omega_\theta \rangle^{+0}$. Although the vorticity advection or vorticity dispersion term acts as a momentum source within the near-wall flow, it is a strong momentum sink within the buffer and overlap regions. Moreover, it is the dominant contribution to TI in and above the log region (Chin *et al.* 2014). As expected by the reader, the premultiplied cospectra of the advective term $\Phi_{u_r \omega_\theta}^{+0}$ does not exhibit any relevant changes between the turbulent base flow and the inertial stage (figures 9*a* and 9*b*).

A snapshot of $\Phi_{u_r \omega_\theta}^{+0}$ at the end of the pretransition (figure 9*c*), at $t^{+0} \approx 90$ shows an energy growth in both, the source and the sink contributions of $\langle u_r \omega_\theta \rangle^{+0}$ especially in the large-scale spectrum. Furthermore, the momentum deficit (blue) region seems to increase in energy earlier than the source contribution.

Along the transition stage, shown in figure 9(*d*), it is possible to note that the momentum source in the advective term experiences substantial growth within the viscous sublayer. Similarly, it is observed a relevant increase in the magnitude of the sink contribution in $\Phi_{u_r \omega_\theta}^{+0}$ from $5 \lesssim y^{+0} \lesssim 15$ at wavelengths $\lambda^{+0} < 100$, which has been encircled (red dashed circle) for clarity. At the same time, it is interesting to notice that a small momentum source is strengthened between $15 \lesssim y^{+0} \lesssim 40$ and $\lambda^{+0} \lesssim 200$. Within the log region, at $40 < y^{+0} < 200$, it is possible to observe the diffusion of the momentum sink within the overlap region of the flow in the small-scale range. This diffusive effect in the negative part of $\langle u_r \omega_\theta \rangle^{+0}$ was not utterly evident in figure 6 (*c*) due to the scale of the plots at the outer flow region. However, the spectrogram of $\Phi_{u_r \omega_\theta}^{+0}$ clearly shows that during the core-relaxation period (figures 9*e* and 9*f*), the negative contributions of the advective term diffuse from the overlap towards the pipe centreline.

Similar to the previous analyses, the difference between two consecutive spectrograms of $\Delta\Phi_{u_r \omega_\theta}^{+0}$ has been conducted and is displayed in figure 10. As expected, the difference between the spectrogram associated with the inertial period and the base flow is depicted in figure 10(*a*) does not show any significant changes.

It is perhaps more interesting to examine $\Delta\Phi_{u_r \omega_\theta}^{+0}$ during the pretransition, exhibited in figure 10(*b*). Firstly, it is observed that both the momentum source and sink contributions mainly grow in energy in the large-scale spectrum ($\lambda^{+0} \gtrsim 1000$ or $\lambda \gtrsim 2R$). The momentum source contribution gains energy in $2 \lesssim y^{+0} \lesssim 9$, showing that throughout the pretransitional period, the LSM and VLSM are responsible for the energy growth
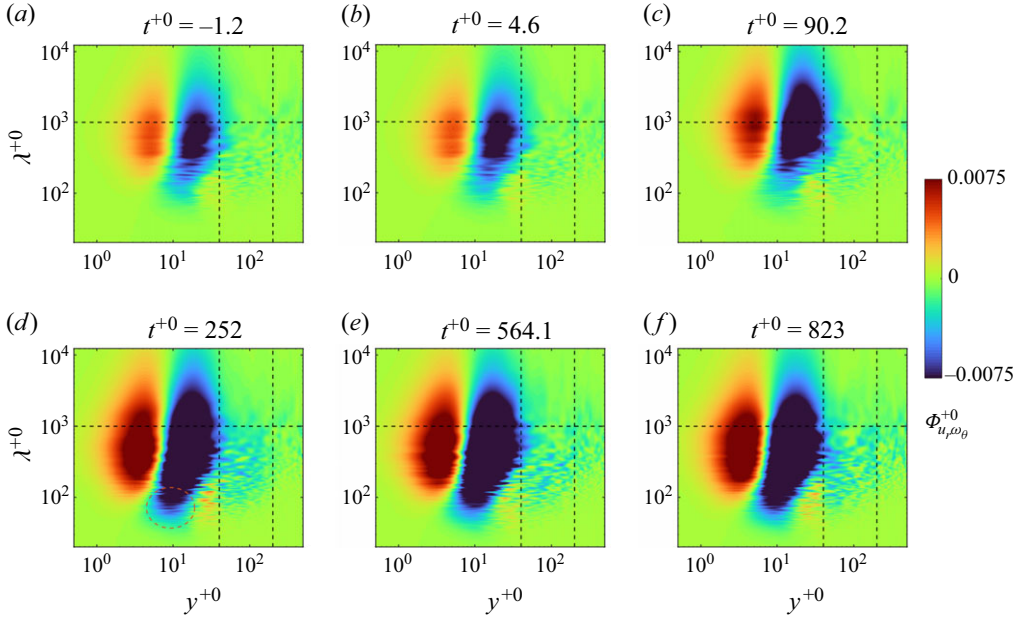
Figure 9. Time evolution of the vorticity advection $\langle u_r \omega_\theta \rangle$ premultiplied cospectra $\Phi^{+0}_{u_r \omega_\theta}$ throughout the different stages undergone by the flow: (*a*) initial steady-state; (*b*) inertial; (*c*) pretransition; (*d*) transition; (*e*) core-relaxation; (*f*) final steady-state.

in the TI. Nevertheless, it is important to notice that the most prominent increase in momentum source at the near-wall region comes from the stretching term (refer back to figure 8*b*). However, a relevant feature observed in $\langle u_r \omega_\theta \rangle^{+0}$ occurs at the buffer region ($10 < y^{+0} < 40$), where the sink term becomes stronger owing to large wavelengths in the range $500 \lesssim \lambda^{+0} \lesssim 12\,500$ ($1 \lesssim \lambda/R \lesssim 8\pi$), revealing that LSM decelerate the mean flow within the buffer region. This is a relevant effect as this momentum sink retards the flow at the buffer to start reshaping the mean velocity profile as shown in figure 1(*b*). It should be mentioned that the physical behaviour observed in the retransition (figure 10*b*) enhances momentum sink observed for large-scale wavelengths of the net force spectra. This will be later discussed in § 4.2.

In figure 10(*b*), it is also noticed that in the small-scale range ($\lambda^{+0} < 300$), and between $10 \lesssim y^{+0} \lesssim 40$, there is a temporary mild growth of a momentum source in the advective term. A momentum source growth also occurs at this location in the stretching term (figure 8*c*). It is important to recall that large-scale stable streaks are produced along the pretransition stage; and, at the end of this period, instabilities appear, and small-scale turbulent spots materialise in the buffer region at the end of the pretransition (see He & Seddighi 2013; He *et al.* 2016; Guerrero *et al.* 2021). Nevertheless, figures 8(*b*) and 10(*b*) reveal that the LSM and VLSM carry out the most relevant role occurring throughout the pretransition.

The energy growth/decrease during the transition period is investigated in figure 10(*c*). Here, it is possible to show that the SSM play a more relevant role during this period. At the near-wall region, it is noticed a growth in a momentum source at the viscous sublayer at wavelengths in the range $100 \lesssim \lambda^{+0} \lesssim 1000$. Adjacent to this momentum source, a region of strong momentum deficit is produced from $5 < y^{+0} < 40$. As explained earlier, these sink regions retard (decelerate) and reshape the mean velocity as a result of the increase in the Reynolds number imposed throughout the flow excursion.
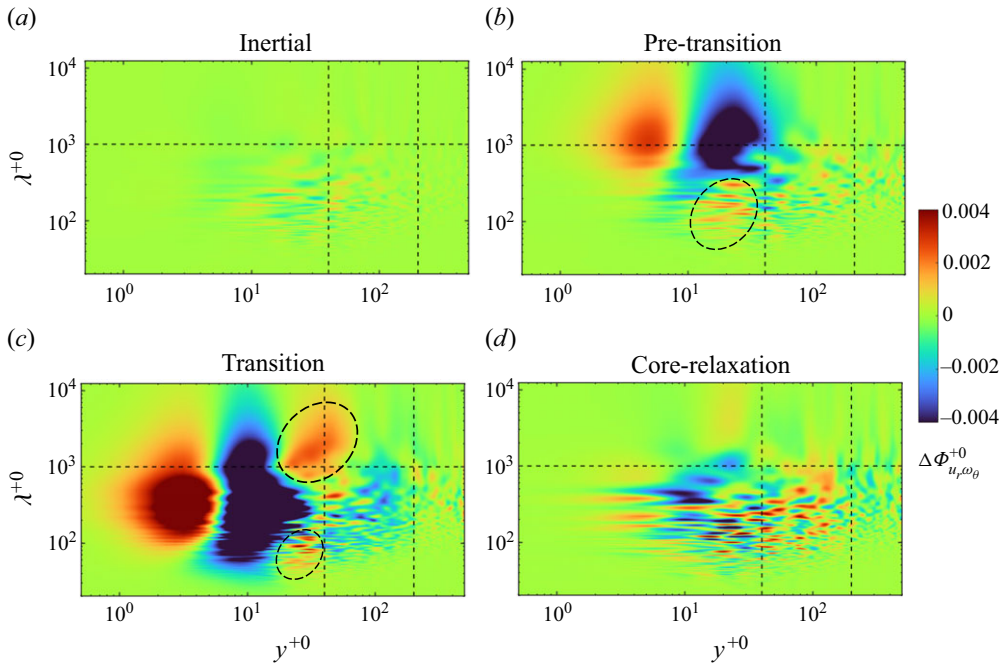
Figure 10. Energy growth in the vorticity advection term $u_r\omega_\theta$ premultiplied cospectra ($\Delta\Phi^{+0}_{u_r\omega_\theta}$) throughout the four transitional stages undergone by an accelerating flow. The energy growth at each stage was obtained by subtracting two consecutive spectrograms from figure 9($a-e$).

The transition stage (figure 10c) also shows two regions where the premultiplied cospectra of $\langle u_r\omega_\theta\rangle^{+0}$ exhibit an energy growth in the buffer region of the flow. These regions are encircled for clarity. More specifically, it is observed that between $20 < y^{+0} < 40$ and in small scales in the range $\lambda^{+0} < 200$, there is a mild energy growth in the turbulent momentum transport. However, it is perhaps more interesting to see that along $20 \lesssim y^{+0} \lesssim 70$ and in the large- and very large-scale spectrum, a momentum source emerges, which most likely contributes to the formation of a region with positive turbulent net force in the buffer region and in very large-scales in the range $\lambda^{+0} > 1500$ in viscous units or $\lambda > 3R$ in outer scale. This region was identified by Wu *et al.* (2012) in their analysis of the net force spectra in steady turbulent pipe flows. However, this region is not evident at friction Reynolds numbers below $Re_\tau \leqslant 500$ (Wu *et al.* 2012; Chin *et al.* 2014). It is also noteworthy that in this same location, the spectra of the stretching term experience an energy decay as previously observed in figure 8(c). The same figure reveals that the small scales, where $\lambda^{+0} < 1000$, produce energy decay, which can also be interpreted as an increase in the magnitude of negative net force within the overlap region of the flow. This implies that SSM act as significant momentum sinks (negative net force) at the overlap region to reshape or flatten the mean velocity profile during the transitional stage.

Finally, the core-relaxation stage, depicted in figure 10(d), shows mild energy growth in the small-scale spectrum at the near wall region. Within the buffer layer, it is possible to note a slight energy decrease in the negative part of $\langle u_r\omega_\theta\rangle$. The overlap region, which interestingly experienced a significant increase in magnitude in the negative net force along the transitional period, shows mild energy growth at the overlap region in the small-scale range. Finally, the core region experiences a slight energy decay at the outer flow region, resulting from a possible advective transport phenomenon of the region with negative net force produced at the overlap region during the transitional stage.

To summarise the observations and results exhibited in this section, the premultiplied cospectra of the velocity vorticity correlations, contributing to the TI or turbulent net force, reveal fascinating behaviours along the transient process of an accelerating turbulent pipe flow. It should be noted that as one would expect, the inertial period does not exhibit relevant changes either in the cospectra of vorticity stretching ($\Phi_{u_\theta\omega_r}^{+0}$) or vorticity advection ($\Phi_{u_r\omega_\theta}^{+0}$), as noted in figures 8(*a*) and 10(*a*). Throughout the pretransition, both the stretching and the advective terms grow in energy in wavelengths of the order $1 \times 10^3 \lesssim \lambda^{+0} \lesssim 1.2 \times 10^4$ or $2R \lesssim \lambda \lesssim 25R$ (see figures 8*a* and 10*b*). This agrees well with previous studies based on flow visualisations (He & Seddighi 2013; Guerrero *et al.* 2021) and reveals that very large scales of the order of 25 pipe radii of length are constituted within the buffer layer and the near-wall region. These flow structures have a significant role in transporting turbulent momentum within $y^{+0} \lesssim 40$ during this stage.

The transition stage shows a complex behaviour, especially in the advective term, shown in figure 10(*c*), where there are regions with positive and negative net force. At the viscous sublayer, a growth in positive net force is noted in the small-scale spectrum; nevertheless, between $5 < y^{+0} < 20$, a growth in the energy of negative turbulent force is noted. At the buffer region and the first part of the overlap layer, a positive growth in turbulent force in the large-scale range is noticed, which seems to be related to the formation of the region E in the net-force spectra, as explained later in §4.2. Similarly, the vorticity stretching $\langle u_\theta\omega_r \rangle^{+0}$ premultiplied cospectra exhibits a growth in positive net force along the transitional stage. It is also relevant to notice that both contributions to the net turbulent force $\langle u_r\omega_\theta \rangle$ and $\langle u_\theta\omega_r \rangle$ exhibit significant growth in the magnitude of negative net force at the overlap region and within the small-scale spectrum. This implies that the mean velocity profile is reshaped in the overlap region along the transitional period due to the increase in the Reynolds number.

Finally, the core-relaxation period shows growth in magnitude in the negative turbulent net force, mainly at the outer flow region in both the advective and stretching contributions to the net force in wavelengths ranging from $100 \lesssim \lambda^{+0} \lesssim 2000$.

4.2. *Net force spectra*

As shown in (4.1), the radial gradient of the Reynolds shear stress plays a significant role in the streamwise mean momentum balance of a canonical turbulent pipe flow, representing the TI or the net force produced by the Reynolds shear stress. Wu *et al.* (2012) explains that the turbulent force can be represented as a function of the wall-normal coordinate ($y = -r$) as

$$\frac{1}{r}\frac{\partial}{\partial r}\left(-r\langle u_r u_z\rangle\right) = \left(\frac{\partial\langle u_r u_z\rangle}{\partial y} + \frac{\langle u_r u_z\rangle}{y-R}\right). \tag{4.4}$$

Wu *et al.* (2012) demonstrated that the Fourier decomposition of the two terms on the right-hand side of (4.4) yields results that are qualitatively similar to those of the first term. In this regard, the wall-normal gradient of the Reynolds shear stress premultiplied cospectrum has been thoroughly investigated in steady turbulent pipe flows (Guala *et al.* 2006; Wu *et al.* 2012; Chin *et al.* 2014) and channel flows (Balakumar & Adrian 2007). The Fourier decomposition of the Reynolds shear stress wall-normal gradient was first introduced by Guala *et al.* (2006) and is expressed as

$$\frac{\partial\langle u_r u_z\rangle^{+0}}{\partial y} = \int_0^\infty \frac{\partial(\Phi_{u_r u_z})}{\partial y}\mathrm{d}\log(\lambda_z^{+0}). \tag{4.5}$$

Equation (4.5), referred to as the net force spectrum, provides insight into how different flow scales contribute to the net turbulent force within the flow. Recently, the net force spectra of canonical pipe flow DNS at moderate (Wu *et al.* 2012) and high-Reynolds numbers (Chin *et al.* 2014; Ahn *et al.* 2017) have been studied. It is also noteworthy that Chin *et al.* (2014) demonstrated that the net force spectrum can be computed by summing the premultiplied cospectra of velocity–vorticity correlations:

$$\frac{\partial \Phi_{u_r u_z}}{\partial y} = \Phi_{u_r \omega_\theta} + \Phi_{u_\theta \omega_r}. \tag{4.6}$$

The net force spectra ($\partial \Phi_{u_r u_z} / \partial y$) have been computed for the accelerating turbulent pipe flow used within this study. Figure 11(*a*–*b*) reveal that the net force spectrum does not suffer any significant changes between the initial steady-state and the inertial period. However, both figures 11(*a*) and 11(*b*) exhibit substantial similarities with the force spectrum analysed by Wu *et al.* (2012), Chin *et al.* (2014) and Ahn *et al.* (2017) at similar Re_τ. Thus, akin to Chin *et al.* (2014), the force spectra have been subdivided into several regions (A to G) where the spectral density (positive or negative) appears to be significant. Within figure 11(*a,b*), it is noted that most of the scales of motion below the buffer layer ($y^{+0} < 30$) work as a momentum source. Most of the contributions within this region mainly come from the stretching term $\Phi_{u_\theta \omega_r}$ (refer back to figure 7*a*). It should also be noticed that throughout the inertial period (figure 11*b*), when the flow excursion takes place, the turbulent scales below the buffer region remain unchanged compared with the turbulent base flow. A similar behaviour occurs along the wall-normal axis and for all the wavelengths captured herein. This provides further evidence that along the inertial period, turbulence remains nearly 'frozen' (Maruyama *et al.* 1976).

It is worthy of mention that a small momentum sink is noted in region A, where very small scales ($\lambda^{+0} < 200$) act. Region A is mainly produced by the negative contribution of $\Phi_{u_r \omega_\theta}$ (refer back to figure 9). As explained by Chin *et al.* (2014), region A comes mainly from positive wall-normal velocities and negative ω_θ at $5 > y^{+0} > 20$ and $\lambda^{+0} \lesssim 120$. This can be understood as clockwise vortical motions being advected in the wall-normal direction, which agrees with the heads of hairpin vortices, near-wall azimuthal vortices or could also be shear layers transported upwards. This behaviour in the context of the vortical motions has been discussed previously by Kline *et al.* (1967) and Kim, Kline & Reynolds (1971) and a recent discussion of the vorticity dynamics in turbulent wall-bounded flows presents a conceptual model for this behaviour (Kumar *et al.* 2023).

Region B is a small momentum source located at $15 < y^{+0} < 60$ and $\lambda^{+0} \lesssim 300$. This region receives most of its contribution from the stretching term $\langle u_\theta \omega_r \rangle$. However, a small positive contribution provides the spectrum of the advective term $\langle u_r \omega_\theta \rangle$ (refer back to figures 7*a* and 9*b*).

Region C is a momentum sink zone that mainly comes from the negative contributions of the $\langle u_r \omega_\theta \rangle$ cospectra between $50 \lesssim y^{+0} \lesssim 200$ and $\lambda^{+0} < 300$. However, it should be noted that the stretching term cospectra also provides a slight negative contribution to this region. Similarly, region D is another relevant sink term, which seems to come from the negative part of $\Phi_{u_r \omega_\theta}$ as observed previously in figure 9. Region D is located between $25 \lesssim y^{+0} \lesssim 70$, and during the initial base flow and the inertial period (figure 11*a*), it corresponds to wavelengths of $300 \lesssim \lambda^{+0} \lesssim 3000$. It should be noted that later studies at $Re_\tau \approx 2000$–3000 (Chin *et al.* 2014; Ahn *et al.* 2017) revealed that region E becomes larger with increasing Re_τ. Within this study, it will be noted that region E becomes evident during the core-relaxation period. However, it will be discussed later.

Region E has values slightly higher than zero during the initial base flow at $Re_\tau \approx 500$. Region E is related to large-scale wavelengths between $4000 \lesssim \lambda^{+0} \lesssim 12\,000$. This agrees with the results provided by Wu *et al.* (2012). All the regions observed for the initial base flow and the inertial period agree with previous studies at similar Reynolds numbers (Wu *et al.* 2012; Chin *et al.* 2014; Ahn *et al.* 2017). Thus, this validates the present results. Hereinafter, the results and time evolution of the force spectra along the pretransition, transition and core-relaxation periods will be analysed.

Figure 11(*c*) reveals several features occurring in the force spectra during the pretransition period. First, it is noticed that the turbulent force experiences slight growth within the viscous sublayer, especially in the large-scale range $\lambda^{+0} > 1000$. This growth is primarily attributed to the positive contributions from $\Delta \Phi_{u_\theta \omega_r}^{+0}$ and $\Delta \Phi_{u_r \omega_\theta}^{+0}$.

Another fascinating feature observed during the pretransition is the emergence of a prominent momentum sink located at $30 \lesssim y^{+0} \lesssim 100$, associated with wavelengths in the range $1 \lesssim \lambda/R \lesssim 8\pi$. The primary contribution to this momentum sink appears to originate from the advective component of the turbulent net force ($\Phi_{u_r \omega_\theta}$). The emergence of this large-scale sink indicates a substantial deviation in the behaviour of region E (refer back to figure 11*c*), which typically acts as a weak momentum source in steady turbulent flows (Wu *et al.* 2012; Chin *et al.* 2014; Ahn *et al.* 2017).

This sink affects the mean momentum balance, reshaping the buffer region of the mean velocity profile by decelerating the flow with a lagged response with respect to the imposed acceleration. The retardation in the mean velocity profile can be attributed to enhanced momentum mixing driven by LSMs and VLSMs in regions D and E of the net force spectra. These structures interact with SSM produced at the inner flow region, as evidenced by the increase in spectral energy density in region B. The large-scale eddies facilitate the transport of high momentum from the outer flow region towards the inner flow region, thereby flattening the mean velocity profile due to the increase in Reynolds number imposed during the inertial period.

Although visualisation of the LSM produced during the transient period is beyond the scope of this work, it could be hypothesised that these LSM and VLSM may be related to elongated flow streaks observed in previous studies (He & Seddighi 2013) surrounded by hairpin-like or quasistreamwise vortical structures produced by the end of the pretransition (Guerrero *et al.* 2021), when instabilities grow and 'new' turbulence is produced within the inner flow region.

The negative contribution of the advective term is the most significant factor responsible for the observed momentum sink (refer back to figures 9*c* and 10*b*). Additionally, the vorticity advection term undershoots the final steady state by the end of the pretransition period, as illustrated in the inset of figure 6(*b*). It should also be noted that the vorticity stretching term is nearly unchanged at $y^{+0} > 40$ (see figures 6*b*, 7*c* and 8*b*). These differences in the temporal response of the velocity–vorticity correlations provide further evidence of the energy redistribution delay undergone by an accelerating turbulent pipe flow (He & Jackson 2000).

Within figure 11(*c*), it is also evidenced that region A has reduced in magnitude while maintaining a negative contribution. It should be noticed that within this location the difference in the cospectra of the velocity–vorticity correlations during the pretransition period (refer back to figures 8*b* and 10*b*) reveals a slight positive energy growth within the same location as region A. Consequently, this region becomes a less relevant momentum sink as the pretransition stage progresses. From a coherent motion perspective, this observation implies a reduction in the population of small-scale near-wall vortices akin to hairpin-like heads occurring during this period. This observation aligns with the findings by He & Jackson (2000), who explain that the large velocity gradients produced at the
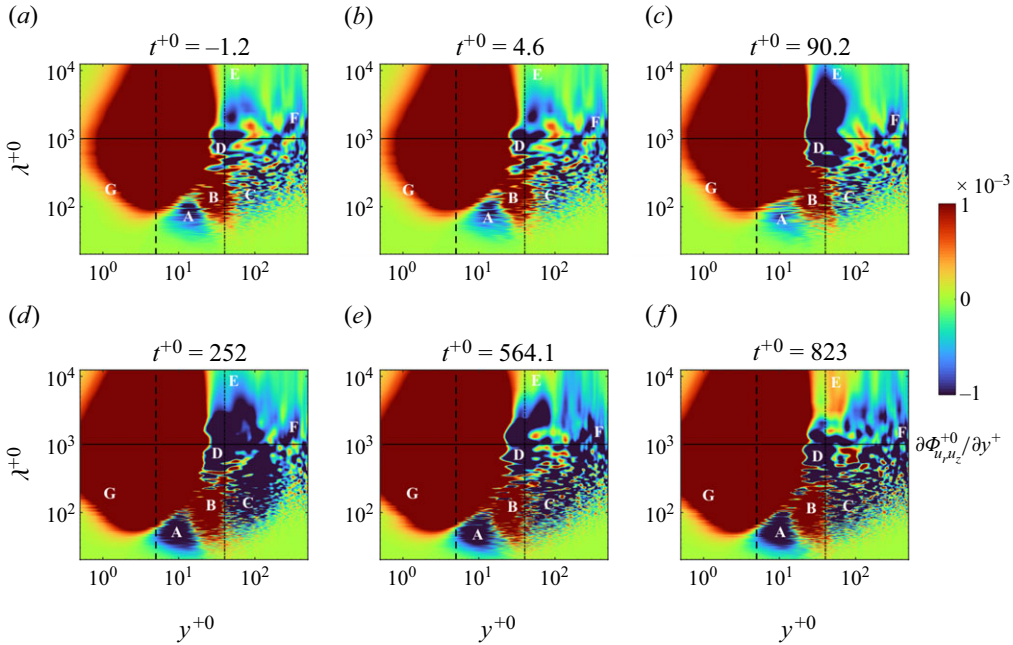
Figure 11. Temporal evolution of the net force spectra $\partial \Phi^+_{u_r u_z}/\partial y$ throughout the different stages undergone by the flow: (*a*) initial steady-state; (*b*) inertial; (*c*) pretransition; (*d*) transition; (*e*) core-relaxation; (*f*) final steady-state. The black solid horizontal line at $\lambda^{+0} = 1000$ represents the threshold used to define the large- and small-scale wavelengths. The vertical dashed and dashed–dot lines are located at $y^{+0} = 5$ and $y^{+0} = 40$, respectively.

near-wall region during this stage tend to stretch the vortices in the streamwise direction. Moreover, Guerrero *et al.* (2021) showed that along the pretransition stage, oblique and quasistreamwise vortices tend to reorient and align axially, evolving into streamwise vortex filaments. These streamwise-aligned vortical structures transport high momentum towards the wall and low momentum from the wall to the core, producing elongated velocity streaks (He & Seddighi 2013).

The small region B, adjacent to A, exhibits a slight energy growth in the small-scale spectrum $\lambda^{+0} < 100$ at $40 \lesssim y^{+0} \lesssim 60$. This energy growth originates from the advective term (figure 9*c*). This observation highlights an increase in the wall-normal transport of azimuthal vorticity. Notably, azimuthal vorticity is closely associated with viscous shear and is generated at the wall by the large velocity gradients induced throughout the flow excursion. However, the 'new' ω_θ layer is transported away from the wall by diffusion and turbulence mixing at a relatively slow pace, reflecting the transient nature of this process.

Figure 11(*d*) exhibits the behaviour of the net force spectra during the transition stage, revealing several interesting features. Firstly, an energy increase is observed in $\partial \Phi_{u_r u_z}/\partial y$ in the momentum source region (region G) located in the viscous sublayer ($y^{+0} < 5$). This growth is primarily attributed to the stretching term $u_\theta \omega_r$, indicating that the mean velocity profile is accelerated at the viscous sublayer; thereby, the velocity gradient at the wall ($\mathrm{d}U_z/\mathrm{d}y$) is increased. This acceleration results from momentum transported from the outer to the inner flow region due to turbulence enhancement. This effect is confirmed in figure 1(*c*), where it is noted that the mean velocity profile at the viscous sublayer is reshaped to recover the well-known linear behaviour related to its final steady-state at the higher Reynolds number attained.

Similarly, figure 11(*d*) indicates an increase in the negative magnitude of region A, showing that this momentum sink strengthens during this transient stage. This negative energy in region A comes mainly from the negative part of the vorticity advection cospectra, $\Phi_{u_r\omega_\theta}^{+0}$ (see figure 10*c*). From a vortical motion perspective, this observation suggests that small-scale azimuthal or hairpin-like head vortices become increasingly significant in the near-wall region during the transition stage. Additionally, turbulent vortices break down into smaller scales. Consequently, region A shifts to shorter wavelengths compared with the inertial and pretransition periods, reflecting the emergence of smaller vortical structures due to the higher Reynolds number attained.

Region B, a momentum source, shows energy growth and extends downwards towards the wall, showing similar behaviour to region A. This positive energy growth in the buffer region on the small-scale range mainly comes from the stretching term, as shown in figure 8(*c*). The energy growth occurring in small-scale wavelengths is related to the breakdown, stretching and enstrophy increase in the flow structures emerging during the transition period (He & Seddighi 2013; Guerrero *et al.* 2021).

During the transition period (figure 11*d*), regions D and E remain merged as a significant momentum sink, occupying a substantial portion of the spectrogram. Indeed, this large-scale momentum sink seems to have diffused radially from the buffer towards the overlap region, spanning $15 \lesssim y^{+0} \lesssim 150$ and is inhabited by flow structures with wavelengths ranging from $300 \lesssim \lambda^{+0} \lesssim 10^4$. The negative behaviour in the force spectra during the transitional period at this wall-normal location is also observed in the inset of figure 6(*c*), where both velocity–vorticity correlations contribute negatively to the TI, providing further evidence of the role of these regions as momentum sinks across the transition period.

It is noteworthy that region E remains predominantly negative until the end of the transition stage. This momentum sink, constituted of large- and very large-scale structures, also plays an essential role in reshaping the mean velocity profile at the same wall-normal location where this sink is observed (refer back to figure 1*c*). Consequently, large- and very large-scale structures decelerate the mean velocity profile at the buffer and overlap regions, commonly observed at the logarithmic region of the flow (Guala *et al.* 2006; Monty *et al.* 2007). As previously explained, during both the pretransition and the transition stages, these large structures act as momentum sinks by transporting momentum from the outer to the inner flow region. This process aids in evolving the mean velocity profile towards its final steady state.

Figure 11(*e*) depicts the force spectra during the core-relaxation period at $t^{+0} = 564.1$. While no significant differences are observed in the near-wall region compared with the transition stage, the buffer and overlap regions reveal modifications, especially in regions D and E. First, region D experiences a notable shrinkage, although it remains a momentum sink. This region is still inhabited by flow structures with wavelengths ranging from $300 \lesssim \lambda^{+0} \lesssim 5000$. Nonetheless, its wall-normal length has substantially reduced as it spans from $15 \lesssim y^{+0} \lesssim 100$. It is also interesting to see a reconstitution in the positive contributions of region E in wavelengths of $O(10^4)$ at $30 \lesssim y^{+0} \lesssim 100$. Despite these changes, the sink term still dominates the force balance between regions D and E.

Finally, $\partial \Phi_{u_r u_z}/\partial y$ has been computed at the final steady-state and is shown in figure 11(*f*). The spectrogram shows that the large- and small-scale wavelengths dominating the large source term across the near-wall region remain nearly unchanged compared with the core relaxation period. A similar trend is exhibited by regions A and B, dominated mainly by SSM. However, region D shows a significant size reduction, now spanning from $15 \lesssim y^{+0} \lesssim 100$ in the wall-normal direction, while its spectral range occurs at $300 \lesssim \lambda^{+0} \lesssim 2000$.

This shrinkage in region D occurs due to the reconstitution and growth of region E. This newly formed momentum source spans from $40 \lesssim y^{+0} \lesssim 200$ and is constituted by large- and very large-scale wavelengths ranging from $2000 \lesssim \lambda^{+0} \lesssim 12000$. Region E plays a critical role during the transition and core-relaxation periods, as it reshapes the mean profile at the overlap region when it becomes negative. This facilitates the attainment of the final steady-state mean velocity profile at a higher Reynolds number. However, during the late core-relaxation period, region E becomes positive again in the large-scale range to balance the forces and prevent the mean profile from continuing to shift downwards (see figures 1*c* and 1*d*).

The present study has provided relevant insights into the evolution of large-scale structures during the transient stages experienced by accelerating pipe flows. Future research employing Fourier filters or proper orthogonal decomposition could offer a deeper extension of this work to further elucidate the time evolution of large-scale structures in a transient context. Such work would complement the present findings and expand our understanding of how large- and very large-scale structures influence the momentum transfer in wall-bounded turbulent flows.

5. Concluding remarks

Direct numerical simulation data of accelerating turbulent pipe flow, following a rapid ramp-up change in Reynolds number, have been analysed to investigate the evolution of LSM and SSM contributing to turbulence production and the variation of TI across the four characteristic stages of this flow.

The premultiplied spectra of the Reynolds shear stress revealed relevant characteristics in each transient stage. During the inertial stage, LSM and SSM contributions exhibit frozen turbulence behaviour. In the pretransition stage, significant energy growth occurs in large-scale wavelengths ($\lambda^{+0}/R \gtrsim 2$) within the buffer region, consistent with the formation of elongated streaks (He & Seddighi 2013). The transition stage is marked by energy growth in both large- and small-scale ranges, with small-scale turbulence growing at a higher rate. Finally, the core-relaxation shows slight growth in LSM and SSM turbulence, predominantly at $y^{+0} > 200$.

A high/low pass Fourier filter has been applied to decompose the Reynolds shear stress and the wall-shear stress $\tau_w(t)$ into LSM and SSM contributions. The large- ($\tau_{w,LS}^T$) and small-scale ($\tau_{w,SS}^T$) turbulence contributions to the frictional drag were quantified using a modified form of the FIK identity (Fukagata *et al.* 2002). The results show that both contributions remain frozen during the inertial stage. During the early pretransition, $\tau_{w,SS}^T$ exhibits slight decay, implying a laminarescent trend, followed by a mild growth towards the end of this period due to the formation of new turbulent spots. Meanwhile, $\tau_{w,LS}^T$, experiences steady growth. During the transition stage, the small-scale turbulent contribution $\tau_{w,SS}^T$ grows much faster than the other terms, becoming the dominant contribution by the end of this period, whereas $\tau_{w,LS}^T$ grows more gradually, experiencing a reduction in the growth rate. Finally, the core-relaxation stage is characterised by slow growth in both the large- and small-scale contributions to τ_w. Notably, small-scale turbulence is the most significant contribution to total frictional drag at the end of the transient flow development.

The premultiplied spectra of the velocity–vorticity correlations have been analysed, focusing on their contributions to the wall-normal gradient of the Reynolds shear stress premultiplied spectra $\partial \Phi_{u_r u_z}/\partial y$, also referred to as the net-force spectra (Guala *et al.* 2006). These correlations represent the stretching $\Phi_{u_\theta \omega_r}$ and the advective $\Phi_{u_r \omega_\theta}$

contributions to the turbulent force (Klewicki 1989). The results shed light on the turbulent scales contributing to the turbulent force or TI in the mean momentum equation. These forces are relevant in reshaping the mean velocity profile throughout the different transient stages undergone by the accelerating pipe flow investigated herein. It is noteworthy that distinct regions (A to F) have been identified in $\partial \Phi_{u_r u_z}^{+0}/\partial y$ similar to previous investigations in steady turbulent flows (Wu *et al.* 2012; Chin *et al.* 2014; Ahn *et al.* 2017). Moreover, the net force spectra analysis helps elucidate how momentum transport is produced across the four transient stages undergone by the accelerating pipe flow investigated herein.

During the inertial stage, the net-force spectra exhibit negligible changes compared with the initial steady-state turbulent base flow, indicating a 'frozen' turbulence response during this period.

In contrast, the pretransition stage manifests significant differences in $\partial \Phi_{u_r u_z}/\partial y$ compared with the steady base flow. In fact, region A, a small-scale sink, reduces in magnitude, implying a reduction in small-scale vortical motions at the near wall region. This phenomenon provides further physical evidence of the 'laminarescent' trend in accelerating flows observed in previous studies (Sreenivasan 1982; He & Seddighi 2013; Guerrero *et al.* 2021). Moreover, a notable growth in the turbulent net force occurs in the inner flow region ($2 \lesssim y^{+0} \lesssim 30$) in large-scale wavelengths ranging from $2 \lesssim \lambda/R \lesssim 8\pi$.

A particularly fascinating finding is the formation of a momentum sink at $30 \lesssim y^{+0} \lesssim 100$, occurring in large- and very large-scale wavelengths. The growth of this sink region results in the expansion of region D while annihilating region E, which is usually a momentum source in steady turbulent wall-flows. The primary contribution to the growth of this momentum sink comes from the advective term $\Phi_{u_r \omega_\theta}^{+0}$. This sink region, occupying regions D and E, signifies momentum mixing produced by LSM and VLSM, which transport momentum from the outer region towards the near-wall region. This process retards and flattens the mean velocity profile in the buffer and overlap regions due to the increase in Reynolds number imposed during the inertial stage. Insights from the spectrogram suggest that the LSM and VLSM associated with this sink region may be related to elongated low-speed streaks surrounded by hairpin pockets (Adrian, Meinhart & Tomkins 2000; Balakumar & Adrian 2007), elongated quasistreamwise vortices (He & Jackson 2000; Guerrero *et al.* 2021) or large-scale roll modes (Hutchins & Marusic 2007; Marusic, Mathis & Hutchins 2010). These structures interact with small-scale vortical motions produced during the pretransition stage, as evidenced by the enhanced spectral energy density in region B. Therefore, the role of this sink region is critical in the transient mean momentum balance of accelerating wall-bounded flows.

During the transition stage, the spectrograms of $\Phi_{u_\theta \omega_r}^{+0}$, $\Phi_{u_r \omega_\theta}^{+0}$ and the net force spectra ($\partial \Phi_{u_r u_z}^{+0}/\partial y$) reveal significant growth in the spectral energy density within the viscous sublayer ($y^{+0} < 5$) and small-scale wavelengths ($\lambda/R \lesssim 2$). This growth implies the generation of 'new' at the wall, characterised by a phase lag (Maruyama *et al.* 1976). The production of this 'new' turbulence predominantly occurs during the transition period. This intensified near-wall momentum source accelerates the mean velocity profile within the viscous sublayer, restoring the well-known linear behaviour.

Simultaneously, the large-scale momentum sink, produced during the pretransition, occupying regions D and E, propagates by diffusion across $30 \lesssim y^{+0} \lesssim 150$ throughout the transition period. By the late transition stage, region E remains a sink, albeit with reduced intensity. This sink continues to enhance momentum mixing through the previously discussed mechanisms, thereby sustaining a retardation effect in the mean velocity profile within the buffer and overlap regions.

Finally, during the core relaxation stage, energy growth is observed in large- and very large-scale wavelengths within the overlap region. This leads to the reconstitution of region E as a momentum source, which becomes evident once the flow attains its final steady state. Consequently, this aids in maintaining a force equilibrium, which results in an establishment in the mean velocity profile at the higher Reynolds number attained.

Declaration of interests. The authors report no conflict of interest.

REFERENCES

ADRIAN, R. 2007 Hairpin vortex organization in wall turbulence. *Phys. Fluids* **19** (4), 041301.

ADRIAN, R., MEINHART, C. & TOMKINS, C. 2000 Vortex organization in the outer region of the turbulent boundary layer. *J. Fluid Mech.* **422**, 1–54.

AHN, J., LEE, J. & SUNG, J.S. 2017 Contribution of lasrge-scale motions to the Reynolds shear stress in turbulent pipe flows. *Intl J. Heat Fluid Flow* **66**, 209–216.

AHN, J., LEE, J.H., LEE, J.K., KANG, J. & SUNG, H.J. 2015 Direct numerical simulation of a 30R long turbulent pipe flow at $Re_\tau = 3008$. *Phys. Fluids* **27**, 065110.

ARIYARATNE, C., HE, S. & VARDY, A. 2010 Wall friction and turbulence dynamics in decelerating pipe flows. *J. Hydraul. Res.* **48** (10), 810–821.

BALAKUMAR, B.J. & ADRIAN, R.J. 2007 Large- and very-large-scale motions in channel and boundary-layer flows. *Phil. Trans. R. Soc. A* **365** (1852), 665–681.

BROWN, G., CHIN, R. & PHILIP, J. 2020 Vorticity transport in turbulent pipe flow. Australasian Fluid Mechanics Conference (AFMC). pp. 1–4. Brisbane, Australia.

BROWN, G., LEE, M. & MOSER, R. 2015 Vorticity transport: the transfer of viscous stress to Reynolds stress in turbulent channel flow. In *Int. Symp. Turbul. Shear Flow Phenom. TSFP*, Melbourne, Australia, pp. 1–6.

CHIN, C., OOI, A.S.H., MARUSIC, I. & BLACKBURN, H.M. 2010 The influence of pipe length on turbulence statistics computed from direct numerical simulation data. *Phys. Fluids* **22** (11), 115107.

CHIN, C., PHILIP, J., KLEWICKI, J., OOI, A. & MARUSIC, I. 2014 Reynolds-number-dependent turbulent inertia and onset of log region in turbulent pipe flows. *J. Fluid Mech.* **757**, 747–769.

CHUNG, Y. 2005 Unsteady turbulent flow with sudden pressure gradient changes. *Intl J. Numer. Meth. Fluids* **47** (8–9), 925–930.

CIOFALO, M. 2022 *Thermofluid Dynamics of Turbulent Flows*. Springer.

EGGELS, J.G.M., UNGER, F., WEISS, M.H., WESTERWEEL, J., ADRIAN, R.J., FRIEDRICH, R. & NIEUWSTADT, F.T.M. 1994 Fully developed turbulent pipe flow: a comparison between direct numerical simulation and experiment. *J. Fluid. Mech.* **268**, 175–210.

FALCONE, M. & HE, S. 2022 A spatially accelerating turbulent flow with longitudinally contracting walls. *J. Fluid Mech.* **945**, A23.

FISCHER, P., LOTTES, J. & KERKEMEIER, S. 2019 Nek5000, Available at https://nek5000.mcs.anl.gov.

FUKAGATA, K., IWAMOTO, K. & KASAGI, N. 2002 Contribution of Reynolds stress distribution to the skin friction in wall-bounded flows. *Phys. Fluids* **14** (11), L73–L76.

GREENBLATT, D. & MOSS, E. 1999 Pipe-flow relaminarization by temporal acceleration. *Phys. Fluids* **11** (11), 3478–3481.

GREENBLATT, D. & MOSS, E. 2004 Rapid temporal acceleration of a turbulent pipe flow. *J. Fluid Mech.* **514**, 65–75.

GUALA, M., HOMMEMA, S.E. & ADRIAN, R.J. 2006 Large-scale and very-large scale motions in turbulent pipe flow. *J. Fluid Mech.* **554** (-1), 521–542.

GUERRERO, B., LAMBERT, M.F. & CHIN, R.C. 2020 Extreme wall shear stress events in turbulent pipe flows: spatial characteristics of coherent motions. *J. Fluid Mech.* **904**, A18.

GUERRERO, B., LAMBERT, M.F. & CHIN, R.C. 2021 Transient dynamics of accelerating turbulent pipe flow. *J. Fluid Mech.* **917**, A43.

GUERRERO, B., LAMBERT, M.F. & CHIN, R.C. 2022 Extension of the 1D unsteady friction model for rapidly accelerating and decelerating turbulent pipe flows. *J. Hydraul. Engng* **148** (9), 04022014.

GUERRERO, B., LAMBERT, M.F. & CHIN, R.C. 2023 Transient behaviour of decelerating turbulent pipe flows. *J. Fluid Mech.* **962**, A44.

HE, K., SEDDIGHI, M. & HE, S. 2016 DNS study of a pipe flow following a step increase in flow rate. *Intl J. Heat Fluid Flow* **57**, 130–141.

HE, S. & JACKSON, J.D. 2000 A study of turbulence under conditions of transient flow in a pipe. *J. Fluid Mech.* **408**, 1–38.

HE, S. & SEDDIGHI, M. 2013 Turbulence in transient channel flow. *J. Fluid Mech.* **715**, 60–102.

HE, S. & SEDDIGHI, M. 2015 Transition of transient channel flow after a change in Reynolds number. *J. Fluid Mech.* **764**, 395–427.

HUTCHINS, N. & MARUSIC, I. 2007 Large-scale influences in near-wall turbulence. *Phil. Trans. R. Soc. A* **365** (1852), 647–664.

JIMÉNEZ, J. 2003 Computing high-Reynolds-number turbulence: will simulations ever replace experiments? *J. Turbul.* **4**, 1–14.

JOEL SUNDSTROM, L.R. & CERVANTES, M.J. 2017 The self-similarity of wall-bounded temporally accelerating turbulent flows. *J. Turbul.* **19** (1), 49–60.

JOEL SUNDSTROM, L.R. & CERVANTES, M.J. 2018 Laminar similarities between accelerating and decelerating turbulent flows. *Intl J. Heat Fluid Flow* **71**, 13–26.

JUNG, S. & CHUNG, Y. 2012 Large-eddy simulation of accelerated turbulent flow in a circular pipe. *Intl J. Heat Fluid Flow* **33** (1), 1–8.

JUNG, S. & KIM, K. 2017 Transient behaviors of wall turbulence in temporally accelerating channel flows. *Intl J. Heat Fluid Flow* **67**, 13–26.

KIM, H., KLINE, S. & REYNOLDS, W. 1971 The production of turbulence near a smooth wall in a turbulent boundary layer. *J. Fluid Mech.* **50** (1), 133–160.

KIM, J., MOIN, P. & MOSER, R. 1987 Turbulence statistics in fully developed channel flow at low Reynolds number. *J. Fluid Mech.* **177**, 133–166.

KLEWICKI, J.C. 1989 Velocity–vorticity correlations related to the gradients of the Reynolds stresses in parallel turbulent wall flows. *Phys. Fluids* **1** (7), 1285–1288.

KLEWICKI, J.C. 2013 A description of turbulent wall-flow vorticity consistent with mean dynamics. *J. Fluid Mech.* **737**, 176–204.

KLINE, S.J., REYNOLDS, W.C., SCHRAUB, F.A. & RUNSTADLER, P.W. 1967 The structure of turbulent boundary layers. *J. Fluid Mech.* **30** (4), 741–773.

KUMAR, S., MENEVEAU, C. & EYINK, G. 2023 Vorticity cascade and turbulent drag in wall-bounded flows: plane Poiseuille flow. *J. Fluid Mech.* **974**, A27.

KUROKAWA, J. & MORIKAWA, M. 1986 Accelerated and decelerated flows in a circular pipe. *Bull. JSME* **29** (249), 758–765.

LIU, X., ZHU, H., BAO, Y., SRINIL, N., ZHOU, D. & HAN, Z. 2024 Time-delayed characteristics of turbulence in pulsatile pipe flow. *J. Fluid Mech.* **979**, A24.

MARUSIC, I., MATHIS, R. & HUTCHINS, N. 2010 Predictive model for wall-bounded turbulent flow. *Science* **329** (5988), 193–196.

MARUYAMA, T., KURIBAYASHI, T. & MIZUSHINA, T. 1976 The structure of the turbulence in transient pipe flows. *J. Chem. Engng Japan* **9** (6), 431–439.

MATHUR, A. 2016 Study of accelerating and decelerating turbulent flows in a channel. *PhD thesis*, The University of Sheffield.

MATHUR, A., GORJI, S., HE, S., SEDDIGHI, M., VARDY, A.E., O'DONOGHUE, T. & POKRAJAC, D. 2018 Temporal acceleration of a turbulent channel flow. *J. Fluid Mech.* **835**, 471–490.

MONTY, J.P., STEWART, J.A., WILLIAMS, R.C. & CHONG, M.S. 2007 Large-scale features in tubulent pipe and channel flows. *J. Fluid Mech.* **589**, 147–156.

MORRILL-WINTER, C. & KLEWICKI, J. 2013 Influences of boundary layer scale separation on the vorticity transport contribution to turbulent inertia. *Phys. Fluids* **25** (1), 015108.

REYNOLDS, O. 1883 An experimental investigation of the circumstances which determine whether the motion of water shall be direct or sinuous, and of the law of resistance in parallel channels. *Phil. Trans. R. Soc. A* **174**, 935–982.

SCOTTI, A. & PIOMELLI, U. 2001 Numerical simulation of pulsating turbulent channel flow. *Phys. Fluids* **13** (5), 1367–1384.

SREENIVASAN, K.R. 1982 Laminarescent, relaminarizing and retransitional flows. *Acta Mech.* **44** (1), 1–48.

TAYLOR, P.S. & SEDDIGHI, M. 2024 Turbulent–turbulent transient concept in pulsating flows. *J. Fluid. Mech.* **982**, A20.

VARDY, A. & BROWN, J. 1995 Transient, turbulent, smooth pipe friction. *J. Hydraul. Res.* **33** (4), 435–456.

VARDY, A. & BROWN, J. 2003 Transient turbulent friction in smooth pipe flows. *J. Sound. Vib.* **259** (5), 1011–1036.

VARDY, A., BROWN, J., HE, S., ARIYARATNE, S. & GORJI, S. 2015 Applicability of frozen-viscosity models of unsteady wall shear stress. *J. Hydraul. Engng* **141** (1), 04014064.

WU, X., BALTZER, J.R. & ADRIAN, R.J. 2012 Direct numerical simulation of a 30R long turbulent pipe flow at $R^+ = 685$: large- and very large-scale motions. *J. Fluid Mech.* **698**, 235–281.

ZIELKE, W. 1968 Frequency-dependent friction in transient pipe flow. *J. Basic Engng* **90** (1), 109–115.